WILEY

FEM×DEM multi-scale model for cemented granular materials: Inter- and intra-granular cracking induced strain localisation

Trung-Kien Nguyen[1] (ID) | **Jacques Desrues[2]** (ID) | **Thanh-Trung Vo[3]** (ID) | **Gaël Combe[2]** (ID)

[1] Faculty of Building and Industrial Construction, Hanoi University of Civil Engineering, Hanoi, Vietnam

[2] University Grenoble Alpes, CNRS, Grenoble, France

[3] Department of Research and International Affairs, Danang Architecture University, Danang city, Vietnam

Correspondence

Trung-Kien Nguyen, Faculty of Building and Industrial Construction, Hanoi University of Civil Engineering, 55 Giai Phong, Road Hanoi, Vietnam.
Email: kiennt3@huce.edu.vn

Abstract

In this paper, we present a multi-scale model that combines the finite element method (FEM) and the discrete element method (DEM) to study the behaviour of cemented granular materials (CGM) at both the sample (macroscopic) and particle (microscopic) scales, taking into account inter- and intra-granular cracking. At the microscopic scale, the material is made up of Volume Elements (VE) composed of particles. Their mechanical behaviour is modelled by the DEM. In the VEs, we find circular grains (single particles) and meso-grains; the meso-grains being made up of clusters of particles linked by strong cohesive bonds. All particles interact via normal/tangential contact and rolling resistance laws with cohesive bonds. At the macroscopic scale, the sample is modelled using the FEM. A VE is assigned to each Gauss point of the mesh; the mechanical response of the VE is used to numerically derive the constitutive response of the material to the strain increment exerted at each point. In the models reported in this paper, localised failures in shear band mode are observed at the macroscopic scale. By performing a microscopic analysis, the results show that the occurrence and development of shear bands give rise locally to a strong evolution of microscopic characteristics such as void ratio, number of contacts (total and debonding contacts), and remarkably by inter- and intra-granular cracking in the case of meso-grains. Furthermore, the stress and strain tensors non-coaxiality is clearly demonstrated inside the shear band, but almost negligible outside.

KEYWORDS

cemented granular materials, inter-intra-granular cracking, micromechanical analysis, multi-scale FEM×DEM, numerical modelling, shear bands

1 | INTRODUCTION

Cemented granular materials (CGM) are of great interest in geomechanics, geoengineering, and civil engineering applications. Typical examples of CGM are concrete, soil-cement mixing, sedimentary rocks,[1,2] even bio-cemented sands.[3] This class of materials has been subjected to numerous theoretical, numerical, and experimental research for a long while.[4–11] In the numerical modelling context, CGM's behaviour could be approached at macro- or micro-scale by either continuum or discrete modelling.[6,9,12] However, each method has its limitations. Continuum modelling (using Finite Element

Method [FEM]) by formulating analytically constitutive models can reproduce the overall behaviour of CGM but meet difficulty in assessing the origin of these macroscopic responses which come from microscopic, that is, the grain scale. On the other hand, it does not seem feasible to model real boundary value problems (BVP) with trillions of particles by discrete modelling (using Discrete Element Method [DEM]).

Bridging the gap between micromechanical studies and continuum approaches at the macro-scale is one of the emergent directions in geomechanics. Among them, since the last decade, true multi-scale modelling by numerical homogenisation method has been developed, named FEM×DEM modelling.[13–19] In this framework, the macro-micro gap is filled by sharing information from the discrete description (by DEM) to the continuum description (by FEM). This innovative approach allows us to model the real scale engineering problem by taking into account the real grain-size at the micro-scale, thus capturing the mechanisms at play across the scales in the simulation of the macro-scale response. The fundamental principle of FEM×DEM approach is to use a Finite Element Model at the macroscopic level to solve real-scale BVP while a Discrete Element Model is used at the microscopic level to describe the real-scale grain-size. The recent FEM×DEM integrated approach has allowed important advances in modelling of failure in cemented geomaterials that take into account micro-structural evolutions and establish the link between behaviours at different scales, leading to the physics that govern material behaviour to be studied at the pertinent scales.

Damage of CGM can be observed at many scales including, engineering scale, laboratory scale, or microscale such as inter-/intragranular cracking. Moreover, failure in CGM is often localised into shear or compaction bands.[1,7,20,21] Significant alteration to mechanical properties can arise with such damage, which can have important implications for the stability and viability of engineering structures. As above discussed, CGM are certainly not homogeneous. Macroscopic behaviour of CGM strongly depends on their nature. Loading and deformation lead to property changes and heterogeneity. Hence it is evident that the microscopic evolution leads to the possible failure of specimens.[16,22,23] However, such effects are not fully understood and are often neglected in modelling.

Failure by strain localisation is really a multi-scale process in which the macro observation is originated from the concentration of micro-mechanisms at smaller scales.[24,25] Such phenomenon requires multiple scales analysis and bridging between them.[17,26–29] It is well known that the strain localisation development in CGM can be considered to be due to the development of microcrack (often classified in inter- and intra-granular cracking of cemented grains) at microscale.[1,23] Several experimental studies[1,20,30] show that strain localisation is associated with grain crushing and huge modification in microstructure and micro-properties.

From a micromechanical standpoint, consideration of damage phenomena at the scale of the grains, that is, inter- and intra-granular cracking, requires multi-scale approach. Despite the recent development of multi-scale approaches mentioned above, this problem has been really tackled only at the grain-scale by Discrete Element Modelling,[9,31–34] without bridging to the macro-scale. Modelling such effects at the grain scale and bridging to the continuum macro scale is still an open question.

Much progress has been made in the FEM×DEM modelling in recent years, in both methodology enhancement and mechanical investigation of granular material/structure: proposing higher-order model and mesh dependency regularization,[17,35,36] 3D macro-micro model development[17,37–39]; studying the model performance and advanced computing scheme[17,19,39,40]; investigating the anisotropy origin/behaviour[41–43]; and application to engineering problems.[41,44–46] However, regarding the particle interaction, most of these later works considered the particles interactions as purely frictional or simple cohesive-frictional law and ignored rolling resistance effect and/or rolling resistance strength, which is not accurately appropriated for CGM. A fully micromechanical model incorporated with normal/tangential and rolling resistance bond is therefore required. Besides, the relationship of macro and micro features in a FEM×DEM multiscale simulation has not been fully studied. More specifically, the relationship between void ratio and the formation and growth of shear bands as recognized in experiments has not been studied in a macro-micro's point of view. The impact of inter- and intra-granular cracking on strain localisation has not been numerically bridged from micro to macro description. Moreover, while coaxiality of the strain and stress tensors is a common assumption of many analytical constitutive laws, it is not observed experimentally.[47,48] With its numerically homogenised constitutive (DEM) law, the FEM×DEM approach allows non-coaxiality to emerge naturally. Also, the evolution of the non-coaxiality angle inside and outside the shear band can be studied and can be given more attention with the FEM×DEM modelling. The objective of this paper is to answer the above questions in the light of the FEM×DEM multi-scale approach.

To this end, a multi-scale model was developed to assess the behaviour of CGM at both macro- and micro-scales, taking into account inter- and intra-granular cracking. The FEM and DEM are integrated into a unified fashion by numerical homogenisation approach. Thanks to the multi-scale framework, we tend to study the pertinent mechanisms of deformation (such as void ratio evolution, non-coaxiality, micro-cracking) at the micro-scale and clarify how they evolve during
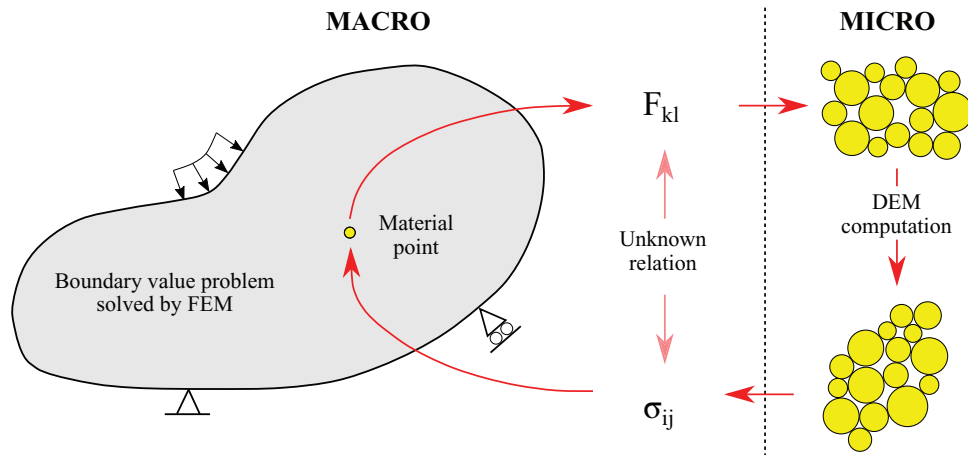
FIGURE 1 FEM×DEM multi-scale modelling: a transition from macro-to micro-scale

a loading process leading to failure. In particular, we aim at capturing the link between microscopic properties changes, and macro-strain localisation initiation and development. Hence the micromechanics features that lead to macro-failure will be assessed and analysed at pertinent scales.

The remainder of this paper is set out as follows: Section 2 presents a multi-scale FEM×DEM model for CGM. Section 3 provides numerical results, along with discussions. Section 4 concentrates on the evolution of microscopic properties that leads to macro-failure. Section 5 points out some conclusions and remarks.

2 | FEM×DEM MODEL FOR CEMENTED GRANULAR MATERIALS

2.1 | Summary of FEM×DEM homogenisation coupling principle

The principle of FEM×DEM method which combines the FEM and the DEM is illustrated in Figure 1.

The BVP is discretized into finite elements. At each Gauss point of the finite elements, a granular assembly (Volume Element [VE]) is assigned. From the deformation gradient tensor assigned to each Gauss point, the associated stress tensor is determined through DEM simulations instead of classical mathematical constitutive equations. The global stiffness matrix of the macroscopic problem is formulated by assembling the element stiffness matrices, to solve incrementally the non-linear finite element problem. The above cycle is repeated for every iteration of the Newton-Raphson iterative method, until satisfying the convergence condition for the current loading step and starting the next one.

In the non-linear analysis by FEM method, the process of solving the non-linear equations system using the Newton-Raphson strategy imposes to determine the Consistent Tangent Operator (CTO) associated with the constitutive response of the material to the strain increment imposed locally. This operator may be derived analytically for simple constitutive laws. However, for advanced constitutive law such as the one in the FEM×DEM method, this operator requires a determination by numerical calculation.[15,16,49] The definition of the CTO is as follows:

$$C_{ijkl} = \frac{\partial \sigma_{ij}}{\partial F_{kl}} \tag{1}$$

For a given increment of deformation gradient δF_{kl}, the stress at the end of the increment is calculated, denoted $\sigma_{ij}(\delta F_{kl})$. Next, perturbation calculations of displacement gradients are considered, which implies in 2D four calculations in applying $\delta F_{kl} + \varepsilon \cdot \Delta_{mn}^{kl}$, where the scalar ε is a small value of perturbation and Δ^{kl} is a second-order tensor whose components are defined by:

$$\Delta_{mn}^{kl} = \delta_{mk} \cdot \delta_{nl} \tag{2}$$

where δ_{mk} is the Kronecker symbol,

$$\begin{cases} \delta_{mk} = 1 \: if \: m = k \\ \delta_{mk} = 0 \: if \: m \neq k \end{cases}.$$

The CTO is then determined by means of stress obtained through perturbation calculations as follows:

$$C_{ijkl} = \frac{\sigma_{ij}\left(\delta F_{kl} + \varepsilon \cdot \Delta_{mn}^{kl}\right) - \sigma_{ij}\left(\delta F_{kl}\right)}{\varepsilon} \tag{3}$$

It can be noted that Equation (3) required five DEM-computations in 2D models and ten DEM-computations in 3D models. When using the DEM-based model to define an equivalent constitutive law on a VE with a limited number of particles, a very common problem to be faced is the scattering of DEM responses for the tiny changes in the strain path imposed by the perturbations $\varepsilon \cdot \Delta_{mn}^{kl}$. This comes from the dynamic feature of DEM and induces some non-representative values of CTO components, resulting in turn to non-convergence of the Newton-Raphson process, particularly when the material has entered into the stress-softening regime.

To overcome this difficulty, various solutions have been proposed in recent studies.[16,17,40,50] Desrues et al.[17] classified these suggestions into three families, including Perturbation based operators, Kruyt operators, and Elastic operators. A comprehensive comparison of these alternative operators can be found in the references.[17,40] In this study, the method proposed in Nguyen et al.,[16] based on perturbation calculation is used. While the specified CTO is derived from the perturbation technique defined by Equation (3), an Auxiliary Elastic Operator (AEO) can be defined as the average CTO obtained in the strain hardening regime of the material's behaviour. In the pre-peak regime, we use CTO for Newton-Raphson method but when entering the peak and post-peak regime, the AEO operator is used and kept constant during the sequel of the computations. In this case, the iterative resolution process for the macroscopic problem enters in the broad range of quasi-Newton methods. Force and displacement conditions are used as convergence criteria in the Newton-Raphson method. The ratio FNORM/RNORM is used for the force condition, where FNORM and RNORM are respectively the norm of the nodal out-of-balance forces and the norm of the nodal reaction forces (forces on the fixed Degrees of Freedom); as for displacements, we use the ratio UNORM/DNORM, where UNORM is the norm of nodal displacements between current and previous iteration, while DNORM is the norm of nodal displacements between current iteration and beginning of the current step.

2.2 | Micromechanical model for CGM

Unlikely cohesionless granular material, the physics of CGM leads to the introduction of bonds between grains; the cement is modelled in the inter-particle contact law as bonds welding the particles together. Microscopically, a cemented contact can resist normal and tangential forces as well as torque.

The following section presents a 2D bonded contact model for idealised granular media made up of discs, incorporating rolling resistance. This contact model consists of normal/tangential/rolling bond strengths that resist normal force, shear force, and moment, respectively. The bonded contact model proposed below is classified as an irreversible type, which means that the bond cannot recover any strength once broken. When the contact force is less than its strength, characterised below by a contact failure criterion, the cemented bond remains intact. When the contact failure criterion is satisfied, the bond is broken. The contact then behaves as an uncemented frictional contact with a rolling resistance.[51–54]

2.2.1 | Unbonded interaction contact model

We first describe the model of interaction for purely frictional particles, not cemented, that is, without cohesion. We consider a pair of 2D circular particles with radii r_i and r_j which are in contact as shown in Figure 2. The micromechanical models described by many authors[16,17,19,55–57] assumed the contact to be reduced into a single point and do not consider resistance to rolling. As a consequence, an unrealistic rolling without sliding phenomenon is often observed for perfectly circular 2D grains. To avoid this, a rolling resistance can be introduced in the contact. This is done by considering that
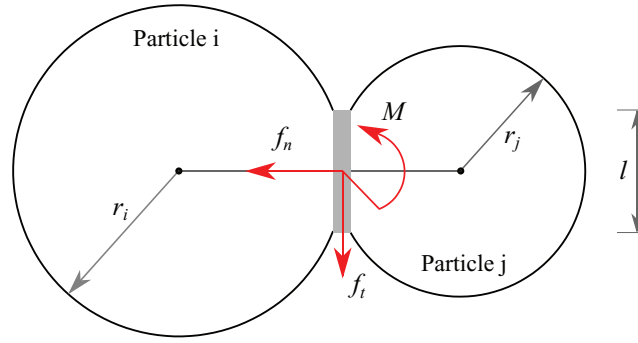
FIGURE 2 A schematic representation of the contact model: interaction force between a couple of grains i and j, composed of normal (f_n), tangential (f_t) forces and moment (M) by rolling resistance effect

the contact is not punctual anymore: the contact between particle occurs through an area, that is, a length in a 2D model (Figure 2).

The rheological model of the contact can be summed up as follows:

(i) *a normal contact force f_n.* The elastic force f_n is proportional to the particles overlap δ. It is supposed to be small compared to grain size.

$$f_n = -k_n \cdot \delta \tag{4}$$

where k_n is the normal stiffness of the contact and $\delta < 0$ when contact occurs.

(ii) *a tangential contact force f_t.* The total tangential force results from a sum of small increments of tangential elastic force Δf_t

$$\Delta f_t = -k_t \cdot \delta u_t \tag{5}$$

where k_t is the tangential stiffness and δu_t is an increment of tangential relative displacement.

For a current time step ΔT, the total tangential force at time $T + \Delta T$ is:

$$f_t^{T+\Delta T} = f_t^T + \Delta f_t^{\Delta T} \tag{6}$$

The tangential force is limited by the Coulomb condition, which implies[52]:

$$|f_t| \leq \mu \cdot f_n \tag{7}$$

The rheological model used to compute the tangential force is thus an incremental elastoplastic law.

(iii) *a rolling resistance M.* Thanks to rolling resistance, the contacts are allowed to transmit to grains a moment M that opposes to rolling. As for the tangential force, the total rolling resistance results from an accumulation of small increment of elastic moment ΔM,

$$\Delta M = -k_r \cdot \delta \theta_r \tag{8}$$

where k_r is the rotational stiffness and $\delta \theta_r$ is an increment of the relative rotation of the two grains in contact.

For a current time step ΔT, the total tangential force at time $T + \Delta T$ is:
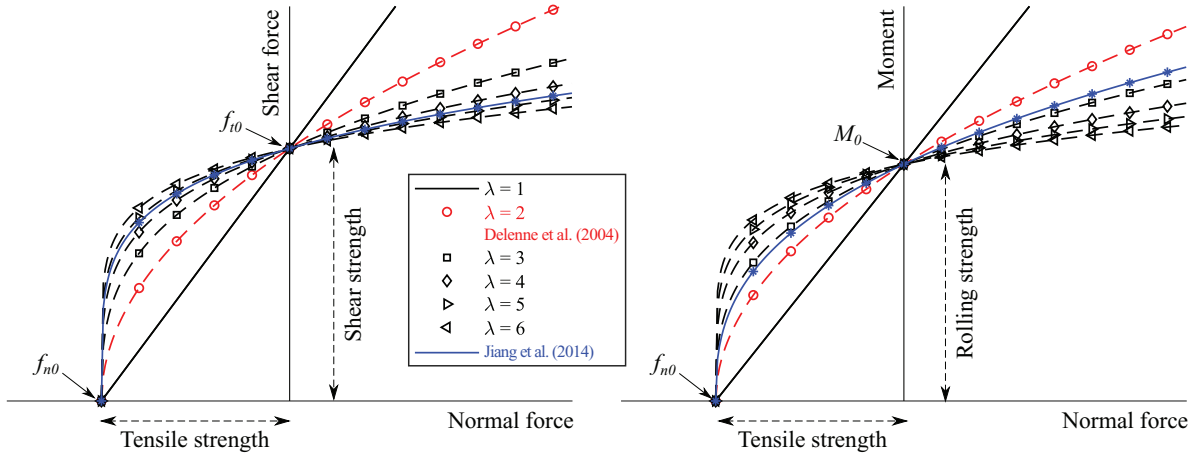
$$M^{T+\Delta T} = M^T + \Delta M^{\Delta T} \tag{9}$$

FIGURE 3 Contact failure criterion displayed as surface envelopes in plans (f_n, f_t) and (f_n, M). f_{n0}, f_{t0}, and M_0 represent the tensile, shear and rolling strength of cemented bonds

This moment is limited by a condition similar to the Coulomb friction:

$$|M| \leq \mu_r \cdot f_n \tag{10}$$

where μ_r is the rolling friction coefficient.[51] It has the dimension of a length. As suggested by,[53,58] k_r and μ_r can be defined by:

$$k_r = k_n \cdot l^2 \tag{11}$$

$$\mu_r = \mu \cdot l \tag{12}$$

where l is the contact length between the two grains; this length represents an elastic deflection of contact. l is defined by $l = 10^{-1} \cdot \bar{a}$, where $\bar{a}$ is the mean diameter of granular assembly.

2.2.2 | Bonded interaction contact model for CGM—Failure criterion

For CGM, a cohesion has to be added between particles in contact. To be representative of a cement, this cohesion must act on the three relative motions of the contact: normal displacement, tangential displacement, and relative rotation. Hence, we need to introduce three cohesions: a normal cohesion (f_{n0}), a tangential cohesion (f_{t0}), and a rotational cohesion (M_0).

These three parameters are gathered together into a unique failure criterion that states if the contact is broken. Once broken, it becomes non-cohesive frictional contact with rolling resistance. The failure criterion is a yield surface in the space of the normal force f_n, the tangential force f_t and the moment M transmitted by the rolling resistance. The failure occurs on the surface $\varsigma = 0$ whereas the intergranular cohesion is maintained inside $\varsigma < 0$. The shape of the failure surface can be tuned according to the criterion exponent coefficients λ.[41,59]

$$\varsigma = \frac{f_n}{f_{n0}} + \left(\frac{f_t}{f_{t0}}\right)^{\lambda} + \left(\frac{M}{M_0}\right)^{\lambda} - 1 \tag{13}$$

Figure 3 shows the criterion shape in the 2D plane (f_n, f_t) and (f_n, M) for various values of λ. For $\lambda = 1$, a linear surface is obtained, and it corresponds to the classical Coulomb criterion with cohesion. In (f_n, f_t) plan, the results of Delenne et al.[60] indicate a parabolic form, equivalent to $\lambda = 2$, while the formulation given in Jiang et al.[61] is more or less similar to the case with $\lambda = 5$. In (f_n, M) plan, the best fit for[61] is $\lambda \approx 3$, while[60] takes the factor of $\lambda = 2$, as in (f_n, f_t) plan. These surfaces pass across the horizontal and vertical axis at the locations corresponding to tensile strength f_{n0}, shear strength f_{t0} and rolling resistance strength M_0. When the criterion is satisfied, the cemented bond is broken,

TABLE 1   Micromechanical model parameters

Parameters	Value
Stiffness level k_n/σ_3	1000
Stiffness ratio k_n/k_t	1
Strength ratio f_{n0}/f_{t0}	1
Intergranular coefficient μ	0.5
Contact length l	$10^{-1} \cdot \bar{a}$
Failure criterion parameter λ	2

in an irreversible manner, that is, if a lost contact is recovered between the two same grains during the modelling, the recovered contact remains a frictional contact with rolling resistance but without cohesion.

The strength ratios f_{t0}/f_{n0} and M_0/f_{n0} are known to depend on the type of cemented materials.[59,62] In the present research, the tensile, shear and moment strengths are evaluated, as suggested by Gilabert et al.,[58] by:

$$f_{n0} = -p^* \cdot (\bar{a} \cdot \sigma_3) \tag{14}$$

$$f_{t0} = \alpha \cdot f_{n0} \tag{15}$$

$$M_0 = \mu_r \cdot f_{n0} \tag{16}$$

where p^* is a dimensionless parameter that rules the importance of the normal cohesion f_{n0} with respect to the average normal compression contact force $(\bar{a} \cdot \sigma_3)$ between particles, where σ_3 is the average pressure exerted on the grain assembly and α is the ratio between the shear and tensile strength. In the case of biaxial loading, as will be discussed later, σ_3 is the confining pressure (a force divided by a length for the 2D case) which is kept constant during the simulations. In this study, micromechanical model parameters were chosen based on numerical efficiency as suggested in the previous works.[16,58,63,64] These DEM parameters used are summed up in the Table 1.

3 | MODELLING BVPS

3.1 | Model set-up and numerical parameters

To demonstrate the capabilities of FEM×DEM multi-scale model in reproducing the behaviour of CGM, simulations of biaxial tests were performed on a sample with a length-to-width ratio of two.

Concerning the VEs, we used the periodic boundary conditions (PBC). The use of a periodic cell allows mechanical responses to be predicted without interaction with rigid boundaries that necessarily imply geometrical constrains. Furthermore, PBC are observed to produce satisfactorily homogeneous, isotropic responses (for isotropic stresses), and the state of static equilibrium.[65–67] The VEs were prepared in a simple manner. Grains were first placed in a periodic box. Then, the intergranular coefficient of friction was set to $\mu = 0.0$ and an isotropic compression (without cohesion) was performed. Intergranular bonds are assigned once the isotropic compression completed and the second isotropic compression with cohesion was conducted.

At the macro scale (the FEM BVP), the biaxial loading was carried out by a displacement-controlled loading while a constant confining pressure was maintained on the left and right boundaries $\sigma_3 = const$. The BVP are described in Figure 4.

The sample low-end was modelled as perfectly smooth to eliminate friction between the lower surface and the sample. The macro-domain (FEM-domain) was discretized by a structural mesh of 5 × 10 quadratic elements using eight nodes and four integration points (Gauss points). Identical VEs were initially assigned to all Gauss integration points.

In this numerical campaign, three BVP biaxial simulations were performed, denoted as CGM1, CGM2, and CGM3. The FEM×DEM condition set-up was similar for three tests except that different VE configurations were used at the microscopic scale (i.e., DEM). The corresponding three VEs are made of the same number of particles, 400. The particles are 2D discs of random sizes of relative radii $r_{max}/r_{min} = 5/3$.

The main difference between these VEs lies in the level of cohesion p^* used in the contacts to bind the grains. For the CGM1 VE, the cohesion is weak, $p^* = 0.5$. For the VE CGM3, the cohesion is strong, $p^* = 2.0$. For the CGM2 VE, these two
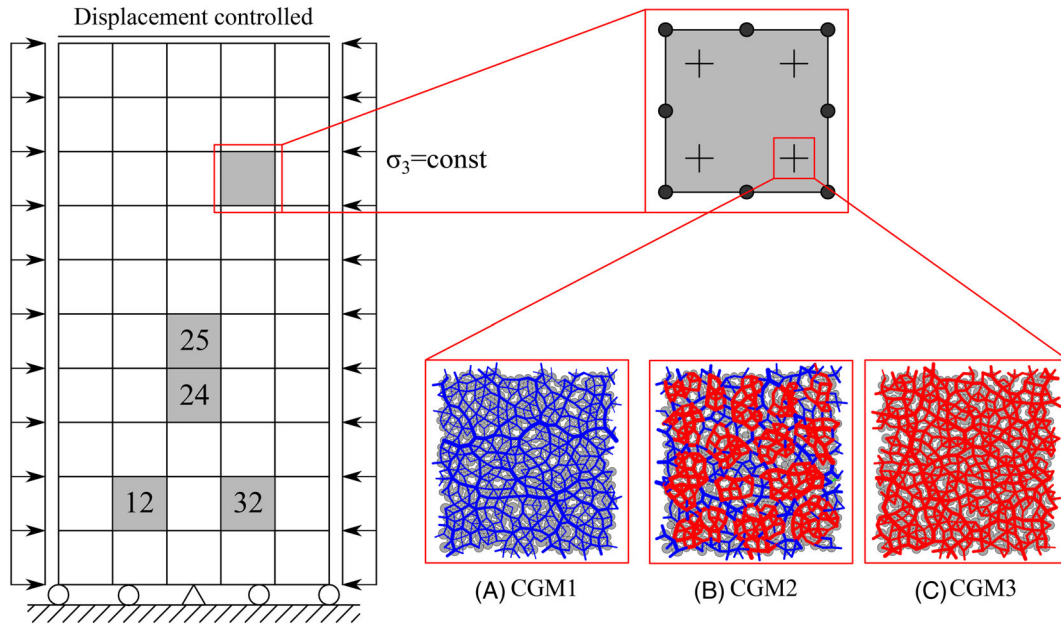
FIGURE 4 FEM×DEM biaxial set-up. The FEM mesh uses 5×10 quadratic elements (eight nodes and four Gauss points). Three cases named CGM1, CGM2 and CGM3 are considered. Each case use VE initially identical at microscopic level. Force chains are displayed with colour conventions: $p^* = 0.5$ in blue and $p^* = 2.0$ in red

TABLE 2 VE microscopic properties of initial DEM-based constitutive model

	Number of particles (npa)	Number of contacts ($ncont$)				Void ratio	Coordination number (z) ($z = \frac{2 \times ncont}{npa}$)
VE		Total	($p^* = 0.0$)	($p^* = 0.5$)	($p^* = 2.0$)		
CGM1	400	837	0	837	–	0.20	4.19
CGM2		822	1	298	523	0.20	4.11
CGM3		840	0	–	840	0.21	4.20

levels of cohesion are used to model a set of fragmentable clusters of grains ($p^* = 2.0$) surrounded by individual particles. To increase the randomness within the cluster of grains, a very few (0, 1, or 2) contact links are allowed to be randomly presented weak bonds inside each cluster. The bounds between (i) different clusters when they are in touch; (ii) individual particles and clusters; and (iii) individual particles themselves, is made of a weak cement ($p^* = 0.5$) (Figure 4). This kind of model aims at introducing the nature of CGM and reproducing the inter- and intra-granular failure. Hereafter we will call the clusters of grains "meso-grains." Microscopic properties of three DEM-based constitutive models are summed up in Table 2.

The FEM×DEM simulations in this present research have been performed using a sequential computing scheme. The computational time is about 60 h for each simulation, slightly higher for CGM2 case. It is worth noting that in the meantime we have also developed more advanced computational frameworks for our FEM×DEM developments, allowing OpenMP and MPI parallel computing schemes to be used. Parallelization helps to considerably speed up the simulations. We invite the readers to refer to Desrues et al.[17] for more details about the numerical implementation and comprehensive comparison of numerical efficiency of different parallel computing schemes.

3.2 | Macro-micro observations

3.2.1 | Stress-strain behaviour

Once the FEM×DEM biaxial modelling performed, one can define normalized deviatoric stress $q/\sigma_3 = (\sigma_1 - \sigma_3)/\sigma_3$ and volumetric strain ε_v versus axial strain ε_{11} at the scale of the specimen. These are the measures used in Figure 5. Several

FIGURE 5 FEM×DEM modelling of biaxial compression tests. Normalized deviatoric stress (q/σ_3) and volumetric strain (ε_v) versus axial strain (ε_{11}) for all simulations. Four zones are distinguished: $\varepsilon_{11} = (0\% - 0.3\%)$ pre-peak regime with quasi-linear behavior; $\varepsilon_{11} = (0.3\% - 1.15\%)$ non-linear pre-peak regime ending up at peak; $\varepsilon_{11} = (1.15\% - 4.0\%)$ post-peak softening phase; $\varepsilon_{11} > 4.0\%$ quasi-constant plateau
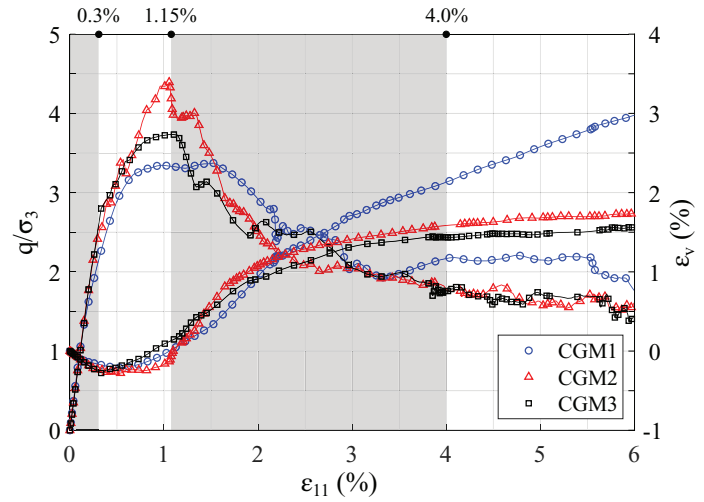
phases can be defined in the response of the specimen:

 (i) quasi-linear phase: at the early loading stage up to 0.3% of axial strain, in the hardening phase, all curves are similar to each other. This can be explained by the behaviour of the VEs: under small deformation, the status of the contacts is essentially within the failure criterion where each contact has an elastic behaviour characterized by k_n, k_t, and k_r, identical for the three VEs. As the three VEs all have an equivalent number of initial contacts, the elastic properties of the contacts being identical, the behaviour of the VEs is very similar, as is the calculation at the macroscopic scale.

 (ii) reaching peak strength: by pursuing the hardening phase, past the quasi-linear phase, the curves diverge to reach a peak, with a different peak stress value—which is logical since the cohesion levels in the three VE cases are different (i.e., CGM1, CGM2, and CGM3); however, at this stage, it is difficult to clearly identify a cross-scale link between the cohesion level (micro) and the peak strength (macro).

(iii) post-peak phase: finally, the deformation proceeds in a softening phase of overall strength reduction, during which the different curves become essentially similar, with some temporary divergences. In trends, it can be noted that the stress-strain curve reaches the same plateau. As we could see later in this paper, this plateau can be associated with the occurrence of a persistent shear band. The response of the specimen is then dominated by this shear band.

Axial and volumetric strains presented in Figure 5 are issued from the overall deformation of the specimen. It can be seen that a typical dilatant behaviour is obtained. In the post-peak regime, before entering the plateau, among the three simulations, the maximum value of dilatancy angle is found in the case of CGM2 VE. While the CGM1 and CGM3 VEs consist of perfectly circular particles, the meso-grains constituted by the brittle clusters of bounded particles behave like large non-circular particles, implying a significant increase in the dilatancy angle. In addition, the non-regular shape of the meso-grains also appears to increase the maximum shear strength. This is consistent with previous studies of the influence of the grain shape on the mechanical behaviour of dense assemblies of cohesionless particles.[68,69]

The peak stress of the CGM2 and CGM3 tests are obtained at almost the same axial strain $\varepsilon_{11} = 1.15\%$, and from $\varepsilon_{11} > 3.5\%$, their behaviours are very similar both in stress-axial strain and volumetric-axial strain relationship. These two simulation responses show a post-peak softening phase up to $\varepsilon_{11} = 4.0\%$ before entering a significantly similar plateau. Nevertheless, the softening is most pronounced in the case of CGM2 (with meso-grains) and less significant in the case of strong cohesion CGM3.

Moreover, it should be noted that the peak stress of CGM2 is not only higher, but also much "sharper," which means that we obtain more "fragile" behaviour with meso-grains, in the sense of the fragile-ductile opposition (brittle-ductile) widely used in rock mechanics.[70] This observation will be further discussed in light of changes in microscopic properties by studying the VEs at the microscopic scale.

3.2.2 | Strain localisation pattern

A representation of the second invariant of the strain tensor at the macro scale indicates that strain localisation is present in the whole three simulations (Figure 6) with shear bands orientations approximately equal to $45^o - 46^o$. Although it
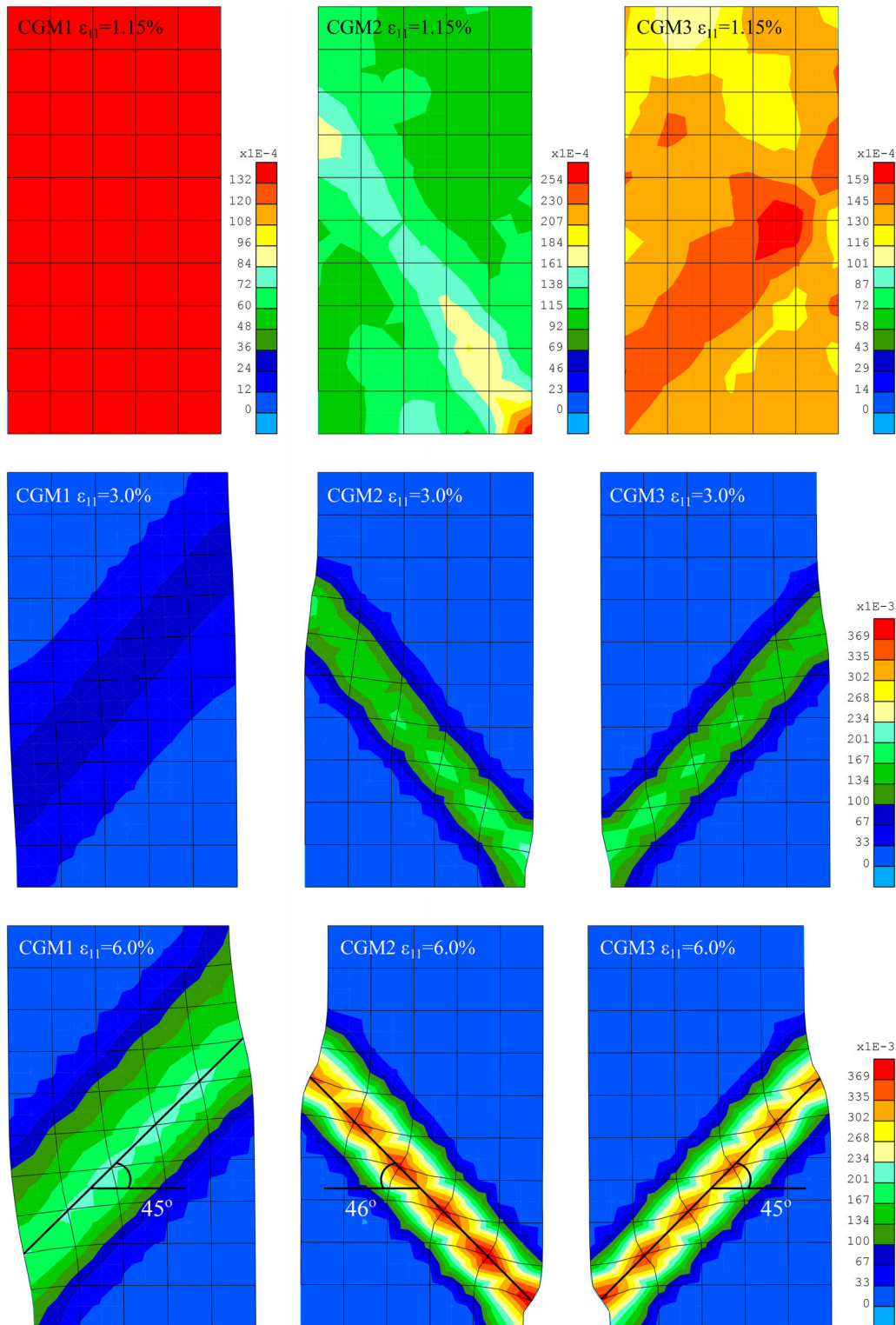
FIGURE 6 Second invariant of strain tensor map for $\varepsilon_{11} = 1.15\%$ (top row), $\varepsilon_{11} = 3.0\%$ (middle row), and $\varepsilon_{11} = 6.0\%$ (bottom row)

may seem that the shear bands are oriented along with the finite element diagonal, previous studies using our multi-scale model have shown that this is not necessarily the case and the inclination of the shear bands can be decorrelated from the mesh,[16] unlike the thickness of the bands; restoring mesh independency for shear band thickness requires the consideration of the second gradient of the deformation, or other higher-order kinematics in the formulation of the finite element problem.[71–75] At $\varepsilon_{11} = 3.0\%$, sample CGM1 is slightly localised, while in samples CGM2 and CGM3 shear band

formation is already very visible. Finally, at $\varepsilon_{11} = 6.0\%$, a larger localised zone is found for the case of weak cohesion (CGM1, $p^* = 0.5$) and the intensity of the deformation concentrated in the band is lower than two other cases (CGM2 and CGM3). Once the strain localisation occurred, the specimen is divided into homogeneous and heterogeneous zones.[21,23]

3.2.3 | Microscopic analyses

The left part of Figure 7 presents the deformed VE microstructures of an integration Gauss point inside the shear band and another outside the shear band as depicted on the right part. Analyses are performed for three different strain levels $\varepsilon_{11} = 0.3\%$ (pre-peak stress level), $\varepsilon_{11} = 1.15\%$ (peak stress level) and $\varepsilon_{11} = 6.0\%$ (post-peak stress level) (Figure 5).

In the hardening phase ($\varepsilon_{11} \leq 0.3\%$), the finite element mesh remains rather homogeneous for the three cases and a shear band is not yet observed. At the micro-scale, it is also observed that, whatever their place in the mesh, the VEs are deformed in a very similar manner for all Gauss points (the VE shape remains rectangular, no shear is observed). Nevertheless, the VE of the CGM1 test (with $p^* = 0.5$) has more broken-bond links (green lines) than in the other cases (CGM2, CGM3).

At $\varepsilon_{11} = 1.15\%$, the shear band is not yet observed for CGM1, while for CGM2 and CGM3, first hints of shear bands allow us to predict their location without them being really developed, Figure 6 (top). As a consequence, the VEs are still submitted to pure diagonal strain tensor, that is, no shear is applied at the microscale and the VE remains rectangular whatever the Gauss point considered. Remembering that, for a given modelling CGM1, CGM2, or CGM3, the initial VEs at each Gauss point are identical, it could be interesting to check if the VE evolution differs from a Gauss point to another. In the Figure 7, it is clearly observed that whatever the chosen Gauss point, the VEs for CGM1 show very similar force maps. Stronger differences can be observed in the VEs of the CGM3 modelling but these differences remain rather modest. For CGM2, there are noticeable differences between the VEs chosen far from the shear band and the VEs taken in the shear band. For the VEs taken in the shear band, the meso-grains seem to be largely destroyed. Outside the band, some meso-grains still appear intact. It is interesting to note that when two cohesion levels coexist in the material, the contacts carrying the lower cohesion seem to behave like fuses and some meso-grains remain.

For $\varepsilon_{11} \geq 1.15\%$, in the softening phase, the loss of homogeneity of the sample gradually increases and the shear bands develop. This is confirmed by the different evolutions of the VE considered. It is interesting to note that from the peak, the VEs outside the band do not vary much in terms of the contact list and cohesive links; only the intensity of force chains changes, corresponding to the decrease of the axial force on the sample in the post-peak phase, which affects the stress at the points situated outside as well inside the shear band. At the plateau of macroscopic response, it can be seen from their shape of the VEs that the VEs in the bands deform differently from the previous phases, namely they present strong rotations and intense shear; cohesion links are completely destroyed in VEs located inside shear bands in CGM1 and CGM3 cases; only two remain for the VE located in the shear band of CGM2.

4 | MULTI-SCALE INSIGHT INTO STRAIN LOCALISATION: MICROSCOPIC ORIGINS

The FEM×DEM gives a unique manner to assess information from inside the shear band with the study of the VEs assigned to the Gauss points of the elements that are located in the shear band observed at the macro-scale. In this section, analyses are concentrated on the CGM2 simulation to highlight the microscopic origin of macro strain localisation.

4.1 | Non-coaxiality in cemented granular materials

Non-coaxiality refers to the deviation between the principal direction of the stress tensor and that of the strain increment tensor. The non-coaxiality angle is defined by angle β as shown in Figure 8. The mathematical description of β is as follows:

$$tan\left(2\theta_p^\sigma\right) = \frac{2\sigma_{13}}{\sigma_{33-}\sigma_{11}} \tag{17}$$

$$tan\left(2\theta_p^\varepsilon\right) = \frac{2d\varepsilon_{13}}{d\varepsilon_{33-}d\varepsilon_{11}} \tag{18}$$
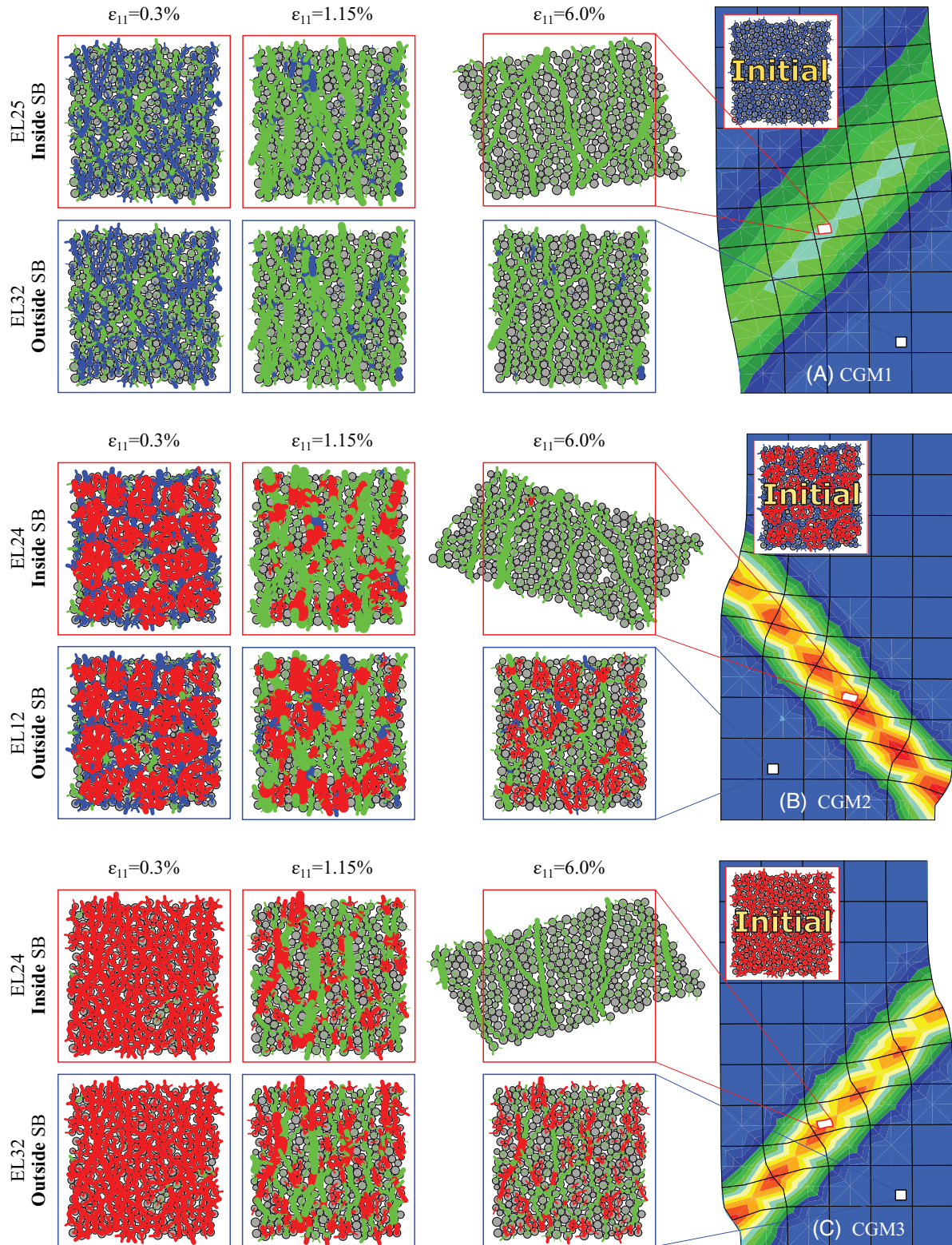
FIGURE 7 Microstructure evolution inside and outside the shear bands of CGM1, CGM2, and CGM3. For each simulation, one VE located outside and one VE inside localised zone are considered. Three instants which correspond to macroscopic axial strain $\varepsilon_{11} = 0.3\%$ (before stress peak), $\varepsilon_{11} = 1.15\%$ (almost stress peak) and $\varepsilon_{11} = 6.0\%$ (almost final instant) are considered. Force chains are drawn with convention: the thickness of the force chain is proportional to the normal force. Cohesionless contacts are plotted in green, contacts with strong cohesion ($p^* = 2.0$) are red and contacts with low cohesion ($p^* = 0.5$) are blue
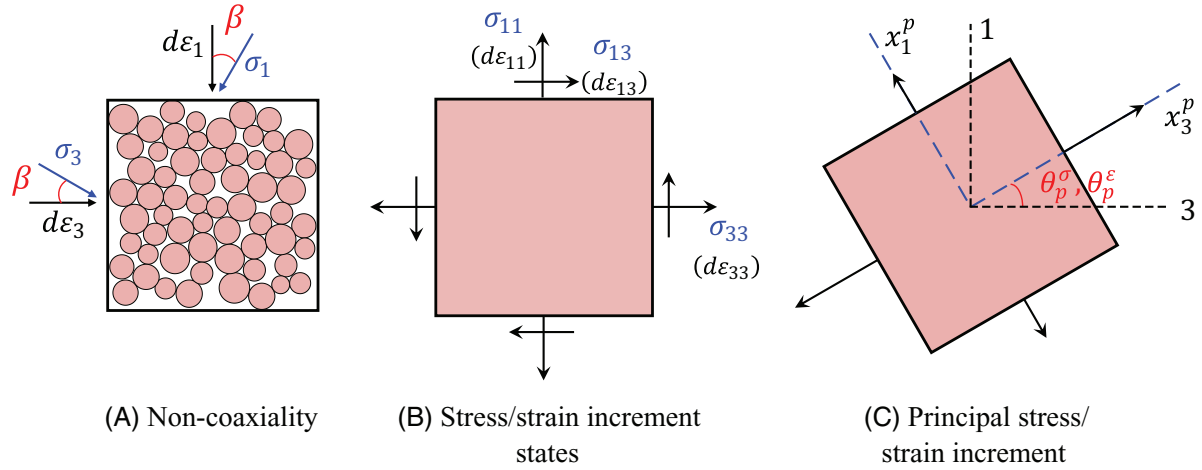
(A) Non-coaxiality (B) Stress/strain increment states (C) Principal stress/ strain increment

FIGURE 8 Definition of principal stress/strain increment angles (B and C) and non-coaxiality angle β (A)

FIGURE 9 Stress cross and shear band for final instant $\varepsilon_{11} = 6.0\%$ of CGM2. Selected elements for non-coaxiality studies are depicted on left figure (Elements 39, 40 outside the shear band and elements 6, 15, 24, 33, 42 along the shear band)
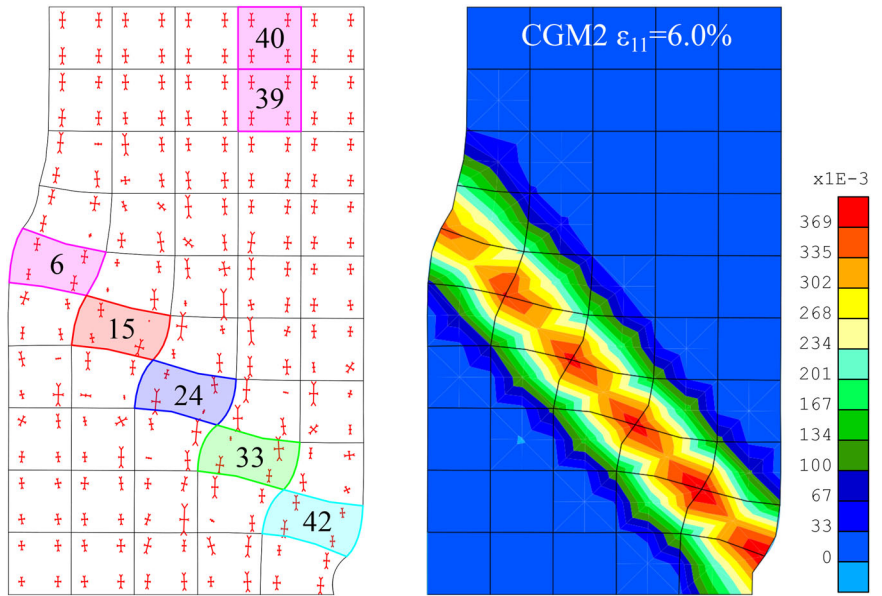
$$\beta = \theta_p^\sigma - \theta_p^\varepsilon \qquad (19)$$

where $\left(\begin{smallmatrix}\sigma_{33} & \sigma_{13}\\ \sigma_{13} & \sigma_{11}\end{smallmatrix}\right)$ is the stress tensor and $\left(\begin{smallmatrix}d\varepsilon_{33} & d\varepsilon_{13}\\ d\varepsilon_{13} & d\varepsilon_{11}\end{smallmatrix}\right)$ the incremental strain tensor. $\theta_p^\sigma, \theta_p^\varepsilon$ define the major principal direction of these two tensors, respectively.

The non-coaxiality in granular materials has been observed commonly, both experimentally and numerically.[42,43,47,48,76–79] This phenomenon naturally relates to the fabric tensor (contact orientation anisotropy) and its evolution in sheared granular materials. So far, most of the constitutive models are formulated based on the assumptions of coaxiality in the principal stress space. Thanks to DEM, the macroscopic behaviour of granular materials is determined through the interactions between particles, describing the discrete nature of such material. The non-coaxiality therefore comes naturally from the microscopic scale (i.e., the granular scale).

Here we propose to study the evolution of the non-coaxiality at the integration points in the case of the CGM2 modelling. We show in Figure 9 the elements for which the non-coaxiality will be assessed. We focus here on the elements identified as being in the shear band. In the same figure (Figure 9), a map of the major and minor stresses and their orientations is shown for $\varepsilon_{11} = 6.0\%$. This map clearly shows that in the shear band and, more surprisingly, in its close vicinity, the principal directions of the stress tensor at the integration points are different from those imposed at the sample boundaries,
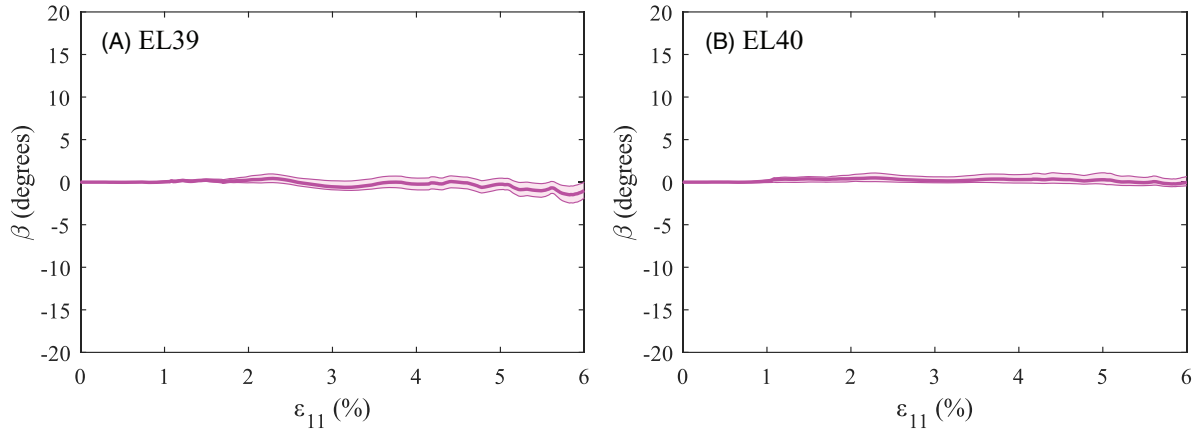
FIGURE 10 Non-coaxiality angle versus macroscopic axial strain in elements 39 (left) and 40 (right) (outside the shear band). The bold continuous line represents the average value of the non-coaxiality angles of each element (over four integration points). The upper and lower envelopes represent the maximum and minimum non-coaxiality angles in the four integration points of such element

that is, major principal stress in the vertical direction, and minor principal stress in the horizontal direction. On the other hand, in areas far from the shear band, the principal stresses have orientations consistent with what would be expected—they are identical to those imposed at the sample boundaries. We checked that the non-coaxiality is not significant in these regions, that is, β is close 0 degrees at the Gauss points (see Figure 10). For the elements of the shear band, β is different from 0 degrees. To illustrate that, the elements 6, 15, 24, 33, 42 are now considered, Figure 9.

On these elements, the angle β is calculated at each Gauss point, throughout the simulation, from $\varepsilon_{11} = 0.0\%$ to $\varepsilon_{11} = 6.0\%$. We show in Figure 11 the evolution of β averaged on the four points of Gauss for the elements 6, 15, 24, 33, and 42. An average over all the elements of the shear band is also shown in Figure 11F.

Surprisingly, one can observe that the β angle fluctuates a lot all along the biaxial compression, whatever the chosen element in the shear band. Secondly, it can be seen that β remains smaller than 2 degrees (in absolute value) for ε_{11} smaller than 1.15%, that is, before the peak of stress. Around the maximum strength, β shows large variations for the non-coaxiality angle, with sudden alternations of increases and drop. One can notice that this also corresponds to the first beginnings of the shear band for the CGM2 modelling. For $\varepsilon_{11} > 1.15\%$, the non-coaxiality angle varies a lot with β ranging from $+25°$ to $-25°$, but the maximum mean value remains in the range $(-12°, 15°)$. Considering the maximum value of the average non-coaxiality angle over the shear band, the range of variation is reduced to $\pm 5°$. The value of β angle is scattered but in general, it shows a significant local non-coaxiality between stress tensor and increment strain tensor. This strong variability of β is hard to understand. Nevertheless, it is possible that the small number of grains (400 particles) used for VEs makes them particularly sensitive to any changes such as changes in the contact network or the breaking of some bonded links. Besides, it should be emphasized that in this study we use a first gradient model at macro-scale (i.e., FEM). Without regularisation by second gradient model, the width of the shear band tends to shrink to a single element size. In such a case, the variation in behaviour between gauss points in the same element is significant. The latter could also explain the strong variability of β. If second gradient model[71,72,80] is used at the macroscale, it is believed that the fluctuation in β would be less important.

The results shown herein indicated that the non-coaxiality angle between the principal directions of the stress tensor and strain increment tensor originates from microscopic evolutions of materials; its evolution is usually neglected with the use of classical constitutive model for granular material. In fact, through the DEM-based constitutive model, the stress tensor is directly computed based on the contacts force network. In the other words, the stress tensor is the result of granular force chains and interparticle displacement. The non-coaxiality is therefore strictly originated from the microstructure and its evolutions.

4.2 | Void ratio and contact direction

To highlight the pertinent mechanisms that lead to global failure of specimens, we investigate in this section the evolution of void ratio and contact direction of VEs located inside the shear band (element 24–EL24) and outside (element 12–EL12).
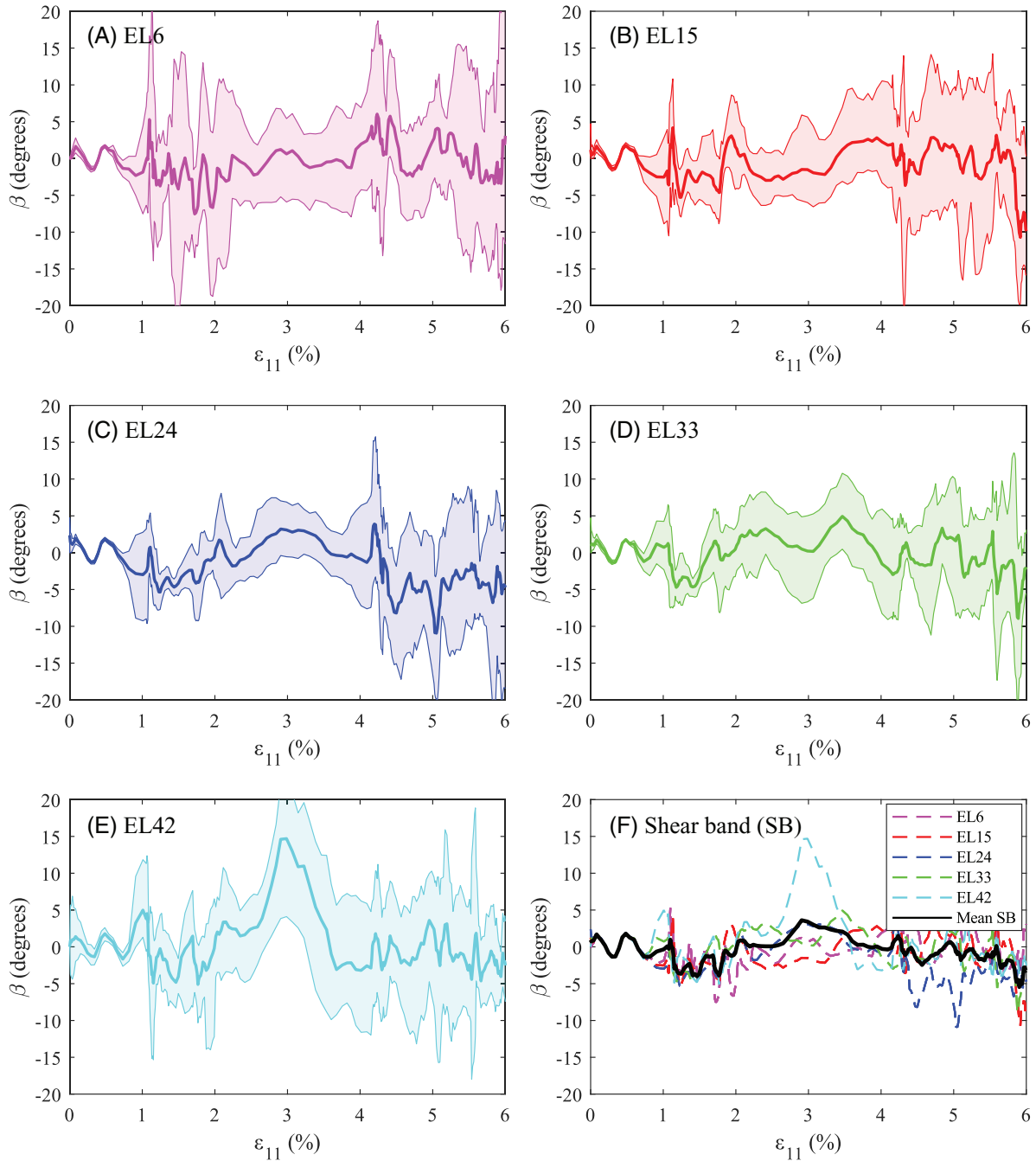
FIGURE 11   Non-coaxiality inside the shear band (CGM2). From (A) to (E): The bold continuous line represents the average value of the non-coaxiality angles of each element (over four integration points). The upper and lower envelopes represent the maximum and minimum non-coaxiality angles among the four integration points of the element. The mean value over the shear band (list of elements 6, 15, 24, 33, 42) is presented in Figure 11F

We propose here to compute for each VE the evolution of the void ratio all along the biaxial test. The void ratio of each of the four VEs of each element is computed and averaged in order to assign a void ratio per element. The void ratio of elements 12 and 24 is shown in Figure 12. In both elements, the void ratio essentially increases along the test, but the void ratio in EL12 changes only slightly in comparison to EL 24 which is located inside the shear band. Figure 12 (right) shows that in both elements, the void ratio does not change significantly before for $\varepsilon_{11} = 1.15\%$, when the maximum strength is reached. Then, the red (inside shear band) and blue (outside) curves diverge, the curve corresponding to the element outside the shear band remaining essentially flat while the one corresponding to inside the shear band shows a fast increase, shortly stopping to reach a plateau around $\varepsilon_{11} = 4.0\%$.
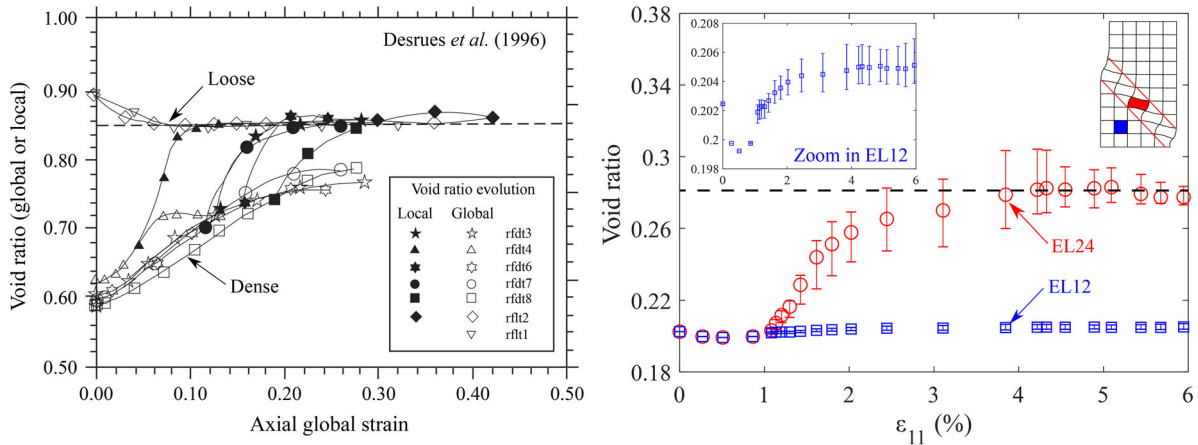
FIGURE 12 Void ratio evolution in presence of strain localisation in compression tests on sand: (left) Experimental observations of void ratio in loose and dense Hostun sand by Desrues et al.[81] and (right) void ratio variations averaged on the Gauss points for elements 12 and 24 (CGM2) versus the overall macroscopic axial strain (ε_{11}). The vertical error bars are the standard deviation around the average
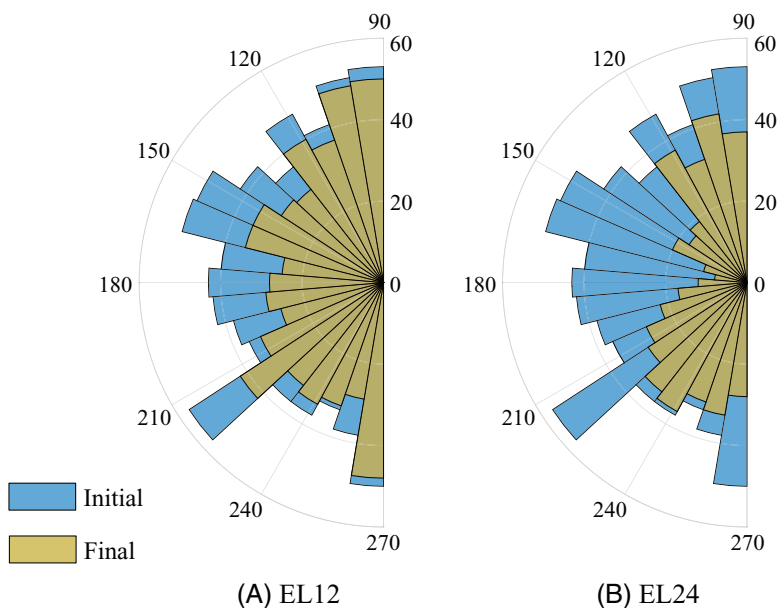

(A) EL12   (B) EL24

FIGURE 13 Contact direction for initial state and final global axial strain of 6.0% (CGM2 case): element 12 (left) and element 24 (right). Angular intervals of ten degrees are used

This local void ratio evolution inside and outside the shear band as shown in Figure 12 (right) is nicely consistent with experimental observations by Desrues et al.,[81] recalled in Figure 12 (left). In both the experimental results and the present numerical results, a limit void ratio is obtained inside the shear band (i.e., EL 24 in this simulation), while the void ratio evolution remains negligible outside, leading the averaged void ratio over the whole specimen to stop its evolution shortly after the full development of strain localisation, at a plateau significantly below the true limit void ratio. This evolution of the overall void ratio and volume change can be observed both in Figure 12 (left) and Figure 5.

Figure 13A,B present the contact directions for the initial and final instants, corresponding to $\varepsilon_{11} = 0.0\%$ and $\varepsilon_{11} = 6.0\%$. The contact direction histogram is determined as the number of normal contacts falling within angular intervals of ten degrees. Comparing the plots (a) and (b) in Figure 13 shows that in EL12, the number of contacts decreased more homogeneously during the biaxial compression than in EL24, despite both VE started from the same initial distribution. In EL24, a strong variation of the contact's direction is observed, and the decreasing is remarkably concentrated in the direction around 180°.

In both elements 12 and 24, it can be seen that the polar histogram loses its isotropy: the anisotropy in contact direction is noticeable. With the growth of anisotropy, the polar histogram takes shape of a peanut which is usually observed in numerical modelling of granular material under biaxial loading.[82,83] Interestingly, as noted above the anisotropy in normal contact direction is much more significant in EL 24, that is, within the shear zone. This confirms that much more contacts
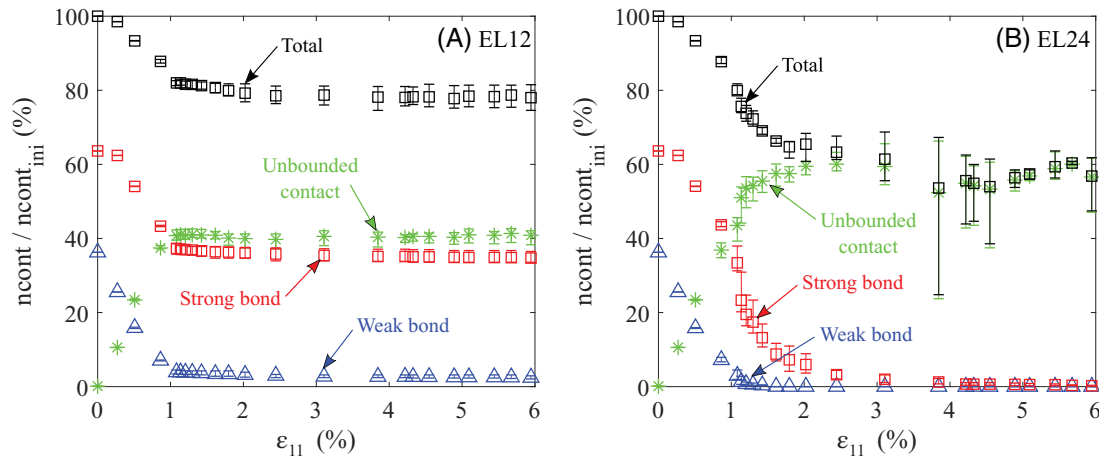
FIGURE 14 Percentage of initial number of contacts (total (black), strong bond (red), weak bond (blue) and unbounded (green)) in elements 12 (left) and 24 (right) versus the macroscopic axial strain (CGM2 case)

are lost in the extension than in the compression direction. This classic result is herein observed to be highly concentrated in the shear band while rather limited outside the shear band.

4.3 | Evolution of contact status and micro-cracking phenomenon

Reinforcing the qualitative results deduced from visual inspection of Figures 7 and 14 quantitatively confirms the evolution of contact status (from bonded to unbounded) inside the element. Regarding the number of contacts, this value decreases in both elements 12 and 24. As displayed in Figure 14A, most of the contacts with low cohesion ($p^* = 0.5$) in EL12 are broken as soon as $\varepsilon_{11} = 1.15\%$; on the other hand, bonded contacts with $p^* = 2.0$ (strong bond) rapidly decreases from the beginning of the simulation till $\varepsilon_{11} = 1.15\%$, then stop evolving. These observations reveal that the elements located outside the shear band change their microscopic feature (number of contacts) only during the hardening phase. Indeed, the maximum stress peak of the specimen corresponds to the emergence of a localised deformation band, in which the degradation of the material concentrates and induces a local drop of the material strength, resulting in a drop of the stress level everywhere in the specimen as soon as the shear band has become a complete deformation mechanism for the structure. In the softening phase, as the stress decreases, forces decrease in every VE in the specimen, not only in the shear band, resulting in an almost complete freeze of strain and micromechanical changes in the VE outside the shear band.

Other observations can be made for EL24 (Figure 14 right). Although in both elements 12 and 24, the total number of contacts decreases and unbounded contacts number increases along the test, it is worth noting that in EL24, passing $\varepsilon_{11} = 3.0\%$, the number of unbounded and total contacts shows up to be equal: in other words, all the contacts are broken. Moreover, as a consequence of the direct link between the number of active contacts and the contact coordination number, the reduction of the total number of contacts shown in Figure 14 implies that in both elements but significantly more in EL24, the contact coordination number has decreased. To summarize, these simple observations clearly show that in the band, the clusters of particles are completely destroyed as soon as ε_{11} reaches 3%. On the contrary, far from the band, the meso-grains (particle clusters) remain essentially intact or little damaged throughout the test.

In the next part of the section, the VEs deformations are studied through their evolutions with an emphasis on the crushing of the meso-grains. The analyses were done by considering several VEs assigned to Gauss points located in an element chosen inside the shear band (EL24), and compared with those of an element located outside (EL12).

As above mentioned, stress-strain behaviour showed first a hardening step before reaching maximal strength at 1.15% of axial strain, then a post-peak regime, during which strain softening occurs with significant reduction of the deviatoric stress. This behaviour can be related to the microscopic features as modelled in the VEs. Microscopic visualisation in terms of normal forces allows to study the occurrence of micro-cracking. At the initial state, every contact is bonded. Along with the loading, the failure criterion can be reached in individual contacts, leading to decohesion between grains at these contacts.
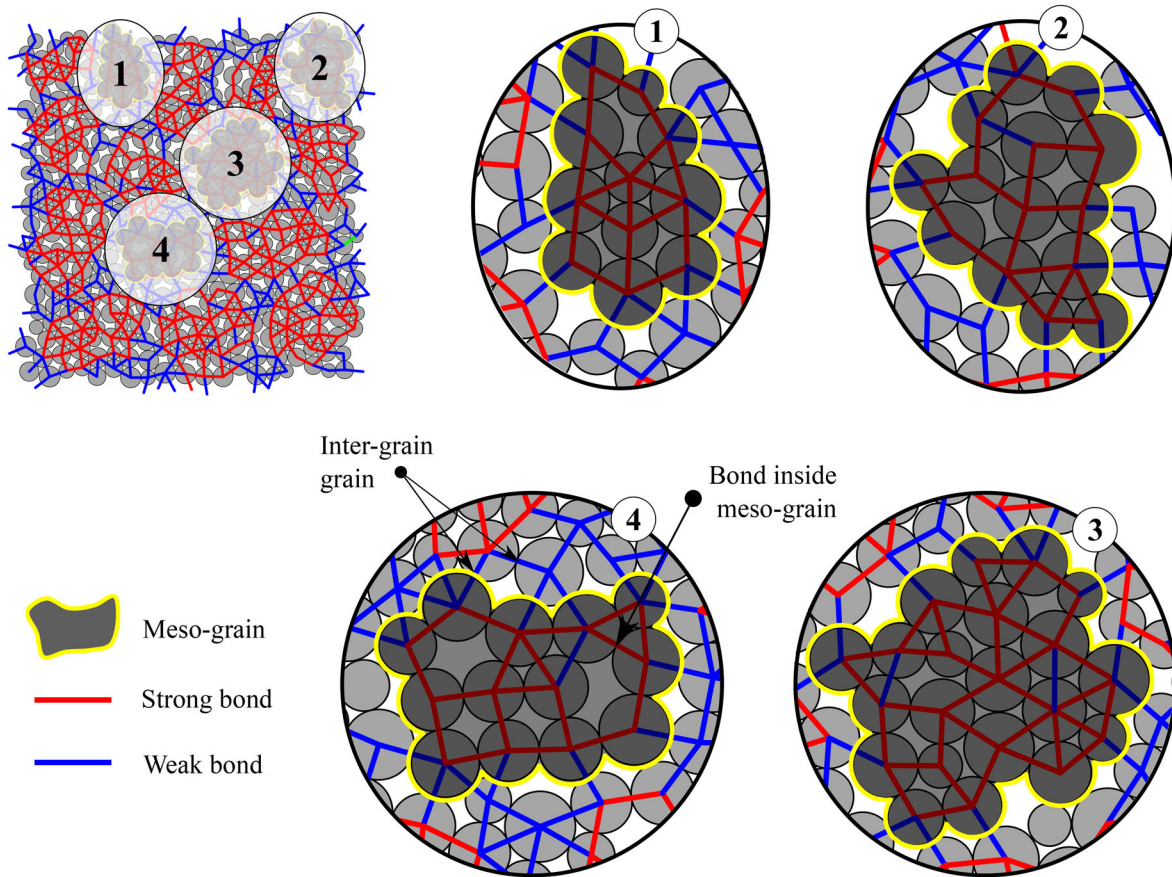
FIGURE 15 Volume element (VE) at initial state showing strong/weak bond and meso-grain. Identical VEs are initially assigned at all Gauss points

The deformation of every VE remains moderate in the pre-peak regime. The normal, shear, and moment at contact point increase along with the loading, which induces micro-damages at grain contacts that spread through VE, a sequence of events that is illustrated in Figure 14B. In the post-peak regime, inside the shear band, the contact decohesion becomes general inside the VE, letting important displacement between grains take place. Indeed, micro-cracking phenomena can be divided into inter- and intra-meso-grain cracking. *Inter-granular cracking* hereafter means the decohesion of bond link between meso-grains or "individual grains" (i.e., grains that do not belong to the meso-grains). In other words, inter-granular cracking takes place at meso-grain boundaries, or individual grain boundaries outside the meso-grains; conversely, *intra-meso-grain cracking* is characterized by the decohesion of the bond links within meso-grains, leading to the disintegration of the meso-grains into smaller fragments. The intra-meso-grain cracking can be triggered from the boundary or the interior of meso-grain.

In the rest of the paper, the following terminology is used: *intra-granular cracking* refers to cracking inside the meso-grains, and *inter-granular cracking* outside, whatever located between simple weakly bonded grains or at individual to meso-grains contacts or even at contacts between meso-grains (all weak bonds anyway).

The coalescence of micro-cracks generates intra-granular cracking through the meso-grain and cracking running through the VE. It can be seen that some cracks occurred due to sliding uniquely while other cracks are open which leads to a global dilatancy. Thus, the global dilative feature of material behaviour is reproduced. At the end of the simulation, the global mechanical responses show a softening state related to micro-cracking at grain contacts. Lower damage corresponds to lower softening of the global microscale response. Different micro-cracking patterns can exhibit at different locations of the sample. The results suggest that the macro strain softening behaviour is related to grain movement, micro-damage, initiation, and propagation of inter- and intra-granular cracking.[84,85]

The initial shapes of meso-grain are given in Figure 15, schematic deformed shapes are illustrated in Figure 15. As a reminder, the VEs are all identical in the initial state at Gauss points, so the meso-grain are all the same as well from one to another VE. Microstructural changes in pre-peak (hardening regime) are mainly related to grain rearrangement
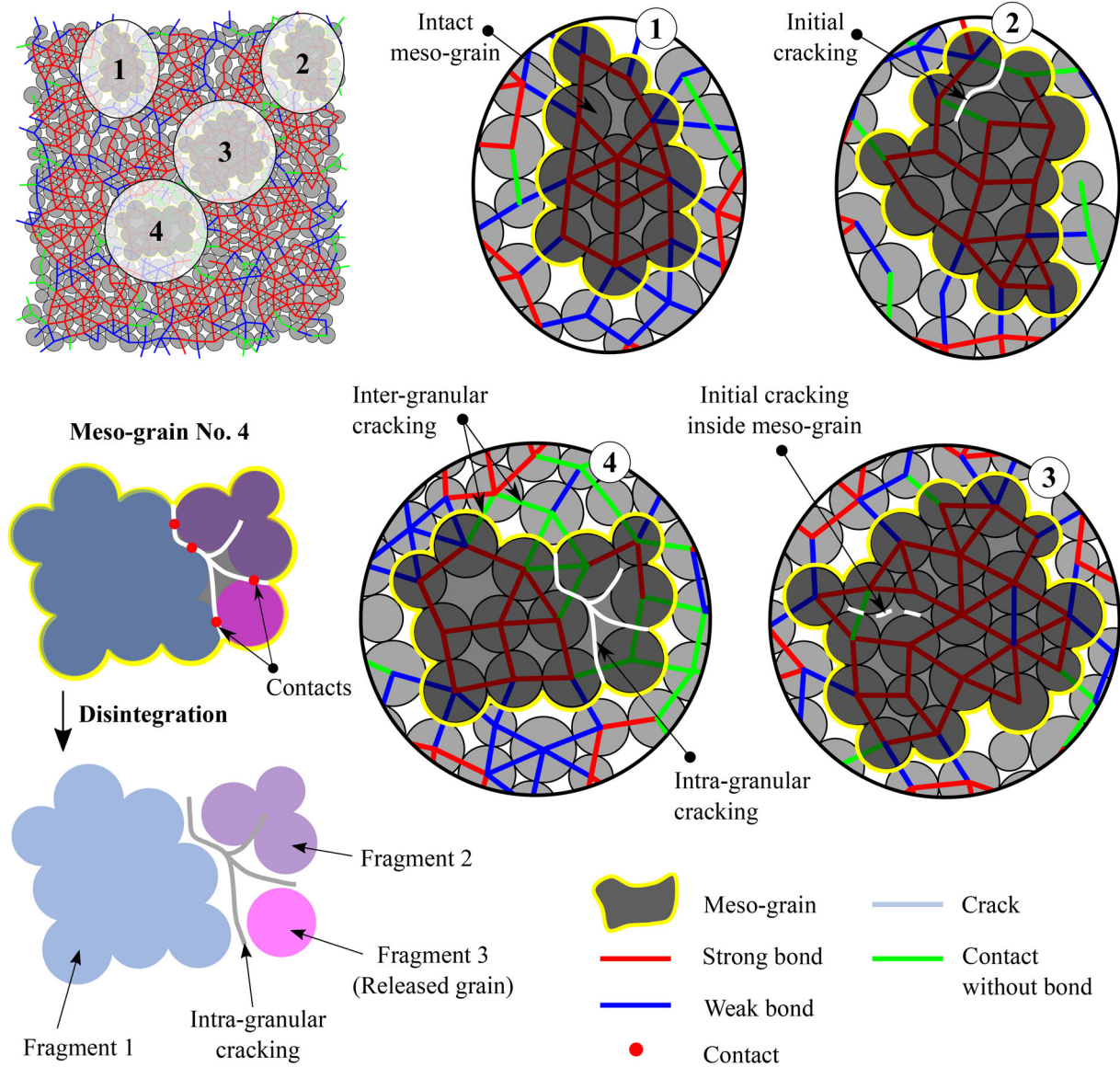
FIGURE 16 Cracking phenomenon inside volume element (VE) (Element 24, inside the shear band of CGM2) at the pre-peak state $\varepsilon_{11} = 0.3\%$. Four meso-grains are considered showing strong/weak bonds and initialisation of both inter- and intra-granular cracking

and inter-granular cracking. However, it can be observed that intra-granular cracking already occurred in one meso-grains during this phase (meso-grain no. 4 in the Figure 16). The propagation of intra-granular cracking leads to the disintegration of the meso-grains into small fragments. As shown in Figure 16, the meso-grain no. 4 is broken into three fragments of different sizes. Among them, the fragment 3 consists of only one single grain while the other two (fragments 1 and 2) are composed of several grains connecting by strong bonds. The fragment consisting of only one single grain is called "released grain" in the rest of the paper.

Figure 17 represents the evolution of selected meso-grains throughout the simulation CGM2 with a focus on EL12 (outside the shear band) and EL24 (inside the shear band). At the pre-peak state ($\varepsilon_{11} = 0.3\%$), the meso-grains are quite similar inside and outside the shear band, with the exception of meso-grain four in which the beginning of a fragmentation process is recognised. Once the stress peak is reached ($\varepsilon_{11} = 1.15\%$), the meso-grains in elements 12 and 24 are affected by fragmentation but differences between 12 and 24 become apparent. As clearly shown in the figure, except the meso-grain no. 1, the fragmentation by intra-granular cracking are observed both inside and outside shear band (for example meso-grains no. 1, 2, 3, 4 in EL24 inside the shear band and meso-grains no. 2, 3, 4 outside the shear band). As for the differences, essentially the fragmentation is more intense inside the shear band. At the peak stress, even the meso-grain shape is similar in elements 12 and 24, there are more "released" grains in element 24 than in element 12, indicating again that the
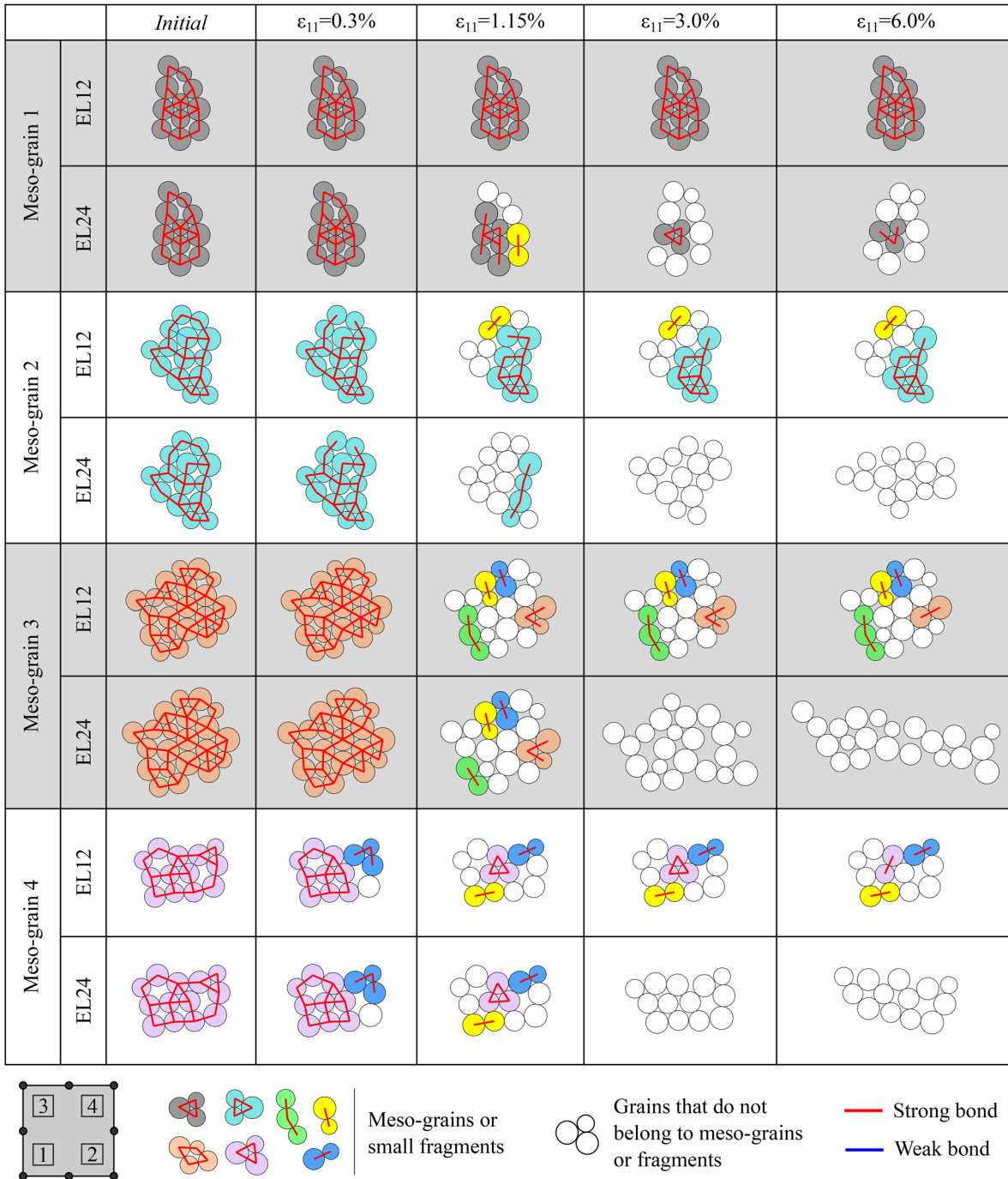
FIGURE 17 Evolution of selected meso-grains of elements 12 (VE-1) and 24 (VE-2). As a result of micro-cracking, the meso-grains are disintegrated into small fragments of several grains and single grains. The initial meso-grains and small-fragment are colored while the released grains that do not belong anymore to meso-grains are shown in white

intra-granular process is more intensive inside the shear band. The shape of meso-grains is better retained outside the shear band, which is in agreement with the evolution of VE shapes. When the specimen's behaviour enters in the softening regime and reaches critical state inside the shear bands, meso-grains no. 2, 3 and 4 in EL24 are completely destroyed in terms of bond and shape: all the grains that constituted these meso-grains have been released by intense cracking. Conversely in element 12, the meso-grains have been broken into a few pieces, but not pulverised as inside the shear band. The disintegration of the meso-grains into small fragments due to intra-granular process, induces loss of stability and strain softening.[1] This allows the small fragments to translate and rotate easier and result in strain localisation. Local

concentration of forces induces the initiation of the cracks discussed above. The crushing effect on large grains surrounded by small ones has been reported in previous studies, for example, Tsoungui et al.[32]

Microstructure evolution related to micro-damage mechanism of bonded granular materials presented above can be summarised as follow. Micro-damage process consists of the development inter-granular cracking first, followed by intra-granular cracking throughout the meso-grains. The initiation and propagation of micro-cracking lead to loss of stability and increasing strain softening of the specimen. This macroscopic aspect is concomitant with void ratio change of such elements as above-mentioned. As loading progresses, the more meso-grains are broken, the more released grains and small fragments are free to rotate and translate.

5 | CONCLUSIONS

The presented FEM×DEM multi-scale model allowed to study the physical and mechanical properties of CGM, involving both a microscopic numerical model and a macroscopic one working concurrently. The microscopic model of granular assembly employed at the micro-scale, was using Discrete Element Modelling, which allows the contact interaction between neighbouring particles to be considered. A specific contact law was adopted to reflect the cementing of the bonds, including normal, tangential, and rolling resistance. The model considered the bond failure between neighbouring particles as irreversible. At the macroscopic level, a non-linear Finite Element Model was used. The main objective of multi-scale modelling is to efficiently bridge scales by numerical homogenisation. In this paper, biaxial compression tests were modelled, exploring three different cases of VE at the micro-scale. The different VEs were defined to describe CGM with varied bond strength. The CGM1 case (resp. CGM3) used weak (resp. strong) bonds everywhere. Conversely, in the CGM2 case, a combination of weak and strong bonds was used, distributed in such a way to define a set of meso-grains in the VE surrounded by weakly bonded individual particles. The introduction of meso-grains in this simple way was shown to effectively describe the macro-strain localisation caused by inter- and intra-granular cracking.

The macroscopic results obtained show that the CGM2 has the highest shear strength. This result is a priori contra-intuitive, since the specimen described by the VE CGM3 with strong bonds everywhere seems a better candidate to give the strongest response. In the present model CGM2, the meso-grains are surrounded by individual particles, however, most meso-grains are directly in contact with other meso-grains. Such an assembly may benefit simultaneously the strength of the meso-grains and some ductility brought by the weak individual particles surrounding them. Based on the present results, it is difficult to validate this tentative explanation. It is one of the perspectives for further work to study the effect of different proportions of meso-grains versus individual grains on the global strength of the specimen modelled; another interesting exploration could be to vary the ratio of the strength of the weak and strong bonds.

Strain localisation is observed in all three cases, but a higher shear intensity is found in CGM2 and CGM3 while a geometrically larger localised shear zone but less intensive is shown in CGM1 case. Multi-scale model FEM×DEM provides a unique way to assess the mechanical behaviour of CGM on both macro and micro scales: the present paper has shown that the microscopic behaviour can be analysed in connection with the macroscopic localisation process by comparing the phenomena occurring in the VEs of different elements located respectively inside and outside the shear bands. The findings reveal that the macroscopic strain localisation has a strong connection with microscopic aspects such as bond breakage, contact orientations, and void ratio of VEs. The following conclusions can be drawn from these concurrent macro-micro analyses:

 (i) Before the stress-strain peak, the coaxiality of the principal strain increment and principal stress direction is observed both inside and outside the shear band; conversely, when the material behaviour enters in the softening phase, non-coaxiality becomes significant in the sheared zones, more than in homogeneous zones.
 (ii) The void ratio evolution is nicely consistent with experimental observations reported in other studies, showing a large jump of dilatancy inside the shear band during the first stage of strain localisation.
(iii) Anisotropy in contact direction is much more significant in the shear band.
(iv) Micro-cracking analysis shows that both inter- and intra-granular cracking occurs in the model involving meso-grains. This has a strong implication in the macroscopic shear strength of materials. It is observed that while the cohesion is completely destroyed for VEs belonging to elements inside the shear band, yet VEs outside the shear band show several (but not all) meso-grains that remain almost intact up to the steady state of the macro simulation.

However, the current development still has some limitations with the use of only 2D FEM×DEM model and the simple up-scaling process which ignores nonlocality or higher order terms. Extending the former one to 3D case is straightforward thanks to our current 3D development model.[17,37,86] Incorporating the fully bonded model into a recent 3D advanced damageable contact law is also planned. Concerning the latter one (i.e., up-scaling process), the use of higher order constitutive framework at the macroscopic level (e.g., second gradient[71]) or other alternative approaches (e.g., size-dependent constitutive modelling framework[87] or strain smoothing technique[36]) would be necessary to mitigate mesh dependency of the thickness of shear bands, as classically observed in numerical modelling of strain localisation. Among them, the second gradient improvement has been implemented without difficulty with our FEM×DEM approach, as demonstrated in Desrues et al.[17] Incorporating this improvement in the present CGM model involving meso-grains is straigthforward, it is among the perspectives of extension of the present study. However, although only a first gradient formulation has been used at the macro-scale (FEM) in this paper, the current results demonstrate the FEM×DEM capability to reproduce and bridge several interesting observations at both macro and micro-scales. Analyses of microscopic properties help to shed light on the origin of macro-phenomena, a major advance brought about by multi-scale approaches and analysis.

DATA AVAILABILITY STATEMENT

The data that support the findings of this study are available from the corresponding author, upon reasonable request.

ORCID

Trung-Kien Nguyen https://orcid.org/0000-0003-0966-1617
Jacques Desrues https://orcid.org/0000-0002-5514-2458
Thanh-Trung Vo https://orcid.org/0000-0003-0259-7165
Gaël Combe https://orcid.org/0000-0002-8633-0793

REFERENCES

1. Fonseca J, Bésuelle P, Viggiani G. Micromechanisms of inelastic deformation in sandstones: an insight using X-ray micro-tomography. *Geotech Lett*. 2013;3(APRIL/JUN):78-83. https://doi.org/10.1680/geolett.13.034.
2. Wang W, Pan J, Jin F, Cui C, Wang B. Effect of cement matrix on mechanical properties of cemented granular materials. *Powder Technol*. 2019;350:107-116. https://doi.org/10.1016/j.powtec.2019.03.040.
3. Dadda A, Geindreau C, Emeriault F, Du Roscoat SR, Filet AE, Garandet A. Characterization of contact properties in biocemented sand using 3D X-ray micro-tomography. *Acta Geotech*. 2019;14(3):597-613.
4. Topin V, Radjai F, Delenne JY. Subparticle stress fields in granular solids. *Phys Rev E - Stat Nonlinear, Soft Matter Phys*. 2009;79(5):1-4. https://doi.org/10.1103/PhysRevE.79.051302.
5. Jiang M, Zhang W, Sun Y, Utili S. An investigation on loose cemented granular materials via DEM analyses. *Granul Matter*. 2013;15(1):65-84. https://doi.org/10.1007/s10035-012-0382-8.
6. Delenne JY, El Youssoufi MS, Cherblanc F, Bénet JC. Mechanical behaviour and failure of cohesive granular materials. *Int J Numer Anal Methods Geomech*. 2004;28(15):1577-1594. https://doi.org/10.1002/nag.401.
7. Bésuelle P, Viggiani G, Lenoir N, Desrues J, Bornert M. X-ray micro CT for studying strain localization in clay rocks under triaxial compression. In: Desrues J, Viggiani G, Bésuelle P, eds. *Advances in X-Ray CT for Geomaterials*. London, Great Britain: ISTE; 2006:35-52.
8. Bésuelle P, Hall SA. Characterization of the strain localization in a porous rock in plane strain condition using a new true-triaxial apparatus. *Springer Series in Geomechanics and Geoengineering*. Heidelberg, London, New York: Springer Dordrecht; 2011. https://doi.org/10.1007/978-94-007-1421-2_46.
9. Shen Z, Jiang M, Thornton C. DEM simulation of bonded granular material. Part I: contact model and application to cemented sand. *Comput Geotech*. 2016;75:192-209. https://doi.org/10.1016/j.compgeo.2016.02.007.
10. Jiang M, Chen H, Crosta GB. Numerical modeling of rock mechanical behavior and fracture propagation by a new bond contact model. *Int J Rock Mech Min Sci*. 2015;78:175-189. https://doi.org/10.1016/j.ijrmms.2015.03.031.
11. Jiang MJ, Yu HS, Harris D. Bond rolling resistance and its effect on yielding of bonded granulates by DEM analyses. *Int J Numer Anal Methods Geomech*. 2006;30(8):723-761. https://doi.org/10.1002/nag.498.
12. Tengattini A, Das A, Nguyen GD, Viggiani G, Hall SA, Einav I. A thermomechanical constitutive model for cemented granular materials with quantifiable internal variables. Part i - Theory. *J Mech Phys Solids*. 2014;70(1):281-296. https://doi.org/10.1016/j.jmps.2014.05.021.
13. Miehe C, Dettmar J. A framework for micro–macro transitions in periodic particle aggregates of granular materials. *Comput Methods Appl Mech Eng*. 2004;193(3-5):225-256.
14. Meier HA, Steinmann P, Kuhl E. Towards multiscale computation of confined granular media: contact forces, stresses and tangent operators. *Tech Mech*. 2007;28(1):32-42.
15. Nitka M, Combe G, Dascalu C, Desrues J. Two-scale modeling of granular materials: a DEM-FEM approach. *Granul Matter*. 2011;13(3):277-281. https://doi.org/10.1007/s10035-011-0255-6.

16. Nguyen TK, Combe G, Caillerie D, Desrues J. FEM × DEM modelling of cohesive granular materials: numerical homogenisation and multi-scale simulations. *Acta Geophys*. 2014;62(5):1109-1126. https://doi.org/10.2478/s11600-014-0228-3.

17. Desrues J, Argilaga A, Caillerie D, et al. From discrete to continuum modelling of boundary value problems in geomechanics: an integrated FEM-DEM approach. *Int J Numer Anal Methods Geomech*. 2019;43(5):919-955. https://doi.org/10.1002/nag.2914.

18. Wu H, Guo N, Zhao J. Multiscale modeling and analysis of compaction bands in high-porosity sandstones. *Acta Geotech*. 2018;13(3):575-599. https://doi.org/10.1007/s11440-017-0560-2.

19. Guo N, Zhao J. A coupled FEM/DEM approach for hierarchical multiscale modelling of granular media. *Int J Numer Methods Eng*. 2014;99(11):789-818.

20. El Bied A, Sulem J, Martineau F. Microstructure of shear zone in Fontainebleau sandstone. *Int J Rock Mech Min Sci*. 2002;39(7):917-932.

21. Desrues J, Bésuelle P, Lewis H. Strain localization in geomaterials. *Geol Soc London, Spec Publ*. 2007;289(1):47-73.

22. van den Eijnden AP, Bésuelle P, Chambon R, Collin F. A FE2 modelling approach to hydromechanical coupling in cracking-induced localization problems. *Int J Solids Struct*. 2016;97-98:475-488. https://doi.org/10.1016/j.ijsolstr.2016.07.002.

23. van den Eijnden AP, Bésuelle P, Collin F, Chambon R, Desrues J. Modeling the strain localization around an underground gallery with a hydro-mechanical double scale model; effect of anisotropy. *Comput Geotech*. 2017;85:384-400. https://doi.org/10.1016/j.compgeo.2016.08.006.

24. Desrues J, Andò E, Mevoli FA, Debove L, Viggiani G. How does strain localise in standard triaxial tests on sand: revisiting the mechanism 20 years on. *Mech Res Commun*. 2018;92:142-146.

25. Andò E, Viggiani G, Desrues J. X-ray tomography experiments on sand at different scales. *Views on Microstructures in Granular Materials*. Switzerland: Springer Nature; 2020:1-20.

26. Li X, Konietzky H, Li X, Wang Y. Failure pattern of brittle rock governed by initial microcrack characteristics. *Acta Geotech*. 2019;14(5):1437-1457.

27. Ma G, Regueiro RA, Zhou W, Liu J. Spatiotemporal analysis of strain localization in dense granular materials. *Acta Geotech*. 2019;14(4):973-990.

28. Bui HH, Nguyen GD. Smoothed particle hydrodynamics (SPH) and its applications in geomechanics: from solid fracture to granular behaviour and multiphase flows in porous media. *Comput Geotech*. 2021;138:104315.

29. del Castillo EM, Neto AHF, Borja RI. Fault propagation and surface rupture in geologic materials with a meshfree continuum method. *Acta Geotech*. 2021;16:2463–2486.

30. Bésuelle P. Compacting and dilating shear bands in porous rock: theoretical and experimental conditions. *J Geophys Res Solid Earth*. 2001;106(B7):13435-13442.

31. Cheng YP, Bolton MD, Nakata Y. Crushing and plastic deformation of soils simulated using DEM. *Geotechnique*. 2004;54(2):131-141.

32. Tsoungui O, Vallet D, Charmet J-C. Numerical model of crushing of grains inside two-dimensional granular materials. *Powder Technol*. 1999;105(1-3):190-198.

33. Bolton MD, Nakata Y, Cheng YP. Micro-and macro-mechanical behaviour of DEM crushable materials. *Géotechnique*. 2008;58(6):471-480.

34. Zhou W, Yang L, Ma G, Xu K, Lai Z, Chang X. DEM modeling of shear bands in crushable and irregularly shaped granular materials. *Granul Matter*. 2017;19(2):1-12. https://doi.org/10.1007/s10035-017-0712-y.

35. Liu Y, Sun W, Yuan Z, Fish J. A nonlocal multiscale discrete-continuum model for predicting mechanical behavior of granular materials. *Int J Numer Methods Eng*. 2016;106(2):129-160.

36. Guo N, Yang Z, Yuan W, Zhao J. A coupled SPFEM/DEM approach for multiscale modeling of large-deformation geomechanical problems. *Int J Numer Anal Methods Geomech*. 2021;45(5):648-667. https://doi.org/10.1002/nag.3175.

37. Nguyen TK, Claramunt AA, Caillerie D, et al. FEM × DEM: a new efficient multi-scale approach for geotechnical problems with strain localization. In: EPJ Web of Conferences. Vol 140; 2017. https://doi.org/10.1051/epjconf/201714011007

38. Guo N, Zhao J. 3D multiscale modeling of strain localization in granular media. *Comput Geotech*. 2016;80:360-372. https://doi.org/10.1016/j.compgeo.2016.01.020.

39. Zhou Q, Xu W-J, Lubbe R. Multi-scale mechanics of sand based on FEM-DEM coupling method. *Powder Technol*. 2021;380:394-407.

40. Argilaga A, Desrues J, Dal Pont S, Combe G, Caillerie D. FEM×DEM multiscale modeling: model performance enhancement from Newton strategy to element loop parallelization. *Int J Numer Methods Eng*. 2018;114(1):47-65. https://doi.org/10.1002/nme.5732.

41. Nguyen TK, Modélisation multi-échelle des matériaux granulaires frottant-cohésifs. Published online 2013.

42. Zhao J, Guo N. The interplay between anisotropy and strain localisation in granular soils: a multiscale insight. *Geotechnique*. 2015;65(8):642-656. https://doi.org/10.1680/geot.14.P.184.

43. Guo N, Chen LF, Yang ZX. Multiscale modelling and analysis of footing resting on an anisotropic sand. *Géotechnique*. 2021:1-13. https://doi.org/10.1680/jgeot.20.p.306. Published online .

44. Guo N, Zhao J. Multiscale insights into classical geomechanics problems. *Int J Numer Anal Methods Geomech*. 2016;40(3):367-390.

45. Desrues J, Nguyen TK, Combe G, Caillerie D, *Fem × Dem Multi-Scale Analysis of Boundary Value Problems Involving Strain Localization*. 2015. https://doi.org/10.1007/978-3-319-13506-9_37

46. Guo N, Zhao J, Sun WC. Multiscale analysis of shear failure of thick-walled hollow cylinder in dry sand. *Geotech Lett*. 2016;6(1):77-82. https://doi.org/10.1680/jgele.15.00149.

47. Joer H, Lanier J, Desrues J, Flavigny E. 1γ2ε: a new shear apparatus to study the behavior of granular materials. *Geotech Test J*. 1992;15(2):129-137.

48. Calvetti F, Combe G, Lanier J. Experimental micromechanical analysis of a 2D granular material: relation between structure evolution and loading path. *Mech Cohesive-Frictional Mater*. 1997;2:121-163.

49. Zienkiewicz OC. *La Méthode Des Éléments Finis*. Paris: McGraw - Hill Inc.; 1979.

50. Kruyt NP, Rothenburg L. Statistics of the elastic behaviour of granular materials. *Int J Solids Struct*. 2001;38(28-29):4879-4899.

51. Iwashita K, Oda M. Rotational resistance at contacts in the simulation of shear band developpement by DEM. *ASCE J Eng Mech*. 1998;124:285-292.

52. Cundall PA, Strack OD. A disrete numerical model for granular assemblies. *Geotechnique*. 1979;29:47-65. https://doi.org/10.1680/geot.1979.29.1.47.

53. Charalampidou E-M, Combe G, Viggiani G, Lanier J, Mechanical behavior of mixtures of circular and rectangular 2D particles. In: *AIP Conference Proceedings*. Vol 1145; 2009;821-824.

54. Magalhães CFM, Atman APF, Combe G, Moreira JG, Jamming transition in a two-dimensional open granular pile with rolling resistance. *arXiv Prepr arXiv150602478*. Published online 2014.

55. Nguyen TK, Desrues J, Combe G, Nguyen DH. A numerical homogenized law using discrete element method for continuum modelling of boundary value problems. *Lect Notes Civ Eng*. 2020;54. https://doi.org/10.1007/978-981-15-0802-8_113.

56. Vo TT, Nezamabadi S, Mutabaruka P, Delenne J-Y, Radjai F. Additive rheology of complex granular flows. *Nat Commun*. 2020;11(1):1-8.

57. Vo T-T, Nguyen CT, Nguyen T-K, Nguyen VM, Vu TL. Impact dynamics and power-law scaling behavior of wet agglomerates. *Comput Part Mech*. 2021:1-14. https://doi.org/10.1007/s40571-021-00427-9. Published online.

58. Gilabert FA, Roux J-N, Castellanos A. Computer simulation of model cohesive powders: influence of assembling procedure and contact laws on low consolidation states. *Phys Rev Lett E*. 2007;75:011303(1-26).

59. Delenne JY, Topin V, Radjai F. Failure of cemented granular materials under simple compression: experiments and numerical simulations. *Acta Mech*. 2009;205(1-4):9-21. https://doi.org/10.1007/s00707-009-0160-9.

60. Delenne J-Y, Youssoufi MSE, Cherblanc F, Bénet J-C. Mechanical behaviour and failure cohesive granular materials. *Int J Numer Anal Methods Geomech*. 2004;28:1577-1594.

61. Jiang M, Liu F, Zhou Y. A bond failure criterion for DEM simulations of cemented geomaterials considering variable bond thickness. *Int J Numer Anal Methods Geomech*. 2014;38(18):1871-1897.

62. Jiang MJ, Sun YG, Li LQ, Zhu HH. Contact behavior of idealized granules bonded in two different interparticle distances: an experimental investigation. *Mech Mater*. 2012;55:1-15. https://doi.org/10.1016/j.mechmat.2012.07.002.

63. Combe G, Roux J-N. Discrete numerical simulations, quasistatic deformation and the origins of strain in granular materials. In: DiBenedetto H, Doanh T, Geoffroy H, Sauzéat C, eds. *Deformation Characteristics of Geomaterials*. Lisse, The Netherlands: Swet and Zeitlinger; 2003:1071-1078.

64. Nguyen TK, Combe G, Caillerie D, Desrues J, Modeling of a cohesive granular materials by a multi-scale approach. In: *AIP Conference Proceedings*. Vol. 1542; 2013. https://doi.org/10.1063/1.4812151

65. Radjai F. Multi-periodic boundary conditions and the contact dynamics method. *Comptes Rendus Mécanique*. 2018;346(3):263-277. https://doi.org/10.1016/j.crme.2017.12.007.

66. Borja RI, Wren JR. Micromechanics of Granular media Part I. *Comput Methods Appl Mech Eng*. 1995:127.

67. Radjai F, Dubois F. *Discrete-Element Modeling of Granular Materials*. USA: Wiley; 2011.

68. CEGEO B, Szarf K, Voivret C, et al. Particle shape dependence in 2D granular media. *EPL (Europhysics Lett)*. 2012;98:44008.

69. Combe G, Nouguier-Lehon C, Azéma E, et al. A benchmark for particle shape dependence. In: *AIP Conference Proceedings*. Vol. 1542; 2013:883-886.

70. Paterson MS. *Experimental Rock Deformation-the Brittle Field*. Berlin - Heidelberg: Springer - Verlag; 1978.

71. Matsushima T, Chambon R, Caillerie D. Large strain finite element analysis of a local second gradient model: application to localization. *Int J Numer Methods Eng*. 2002;54:499-521.

72. Chambon R, Caillerie D, Matsuchima T. Plastic continuum with microstructure, local second gradient theories for geomaterials: localization studies. *Int J Solids Struct*. 2001;38(46-47):8503-8527. https://doi.org/10.1016/S0020-7683(01)00057-9.

73. Vardoulakis I, Aifantis EC. A gradient flow theory of plasticity for granular materials. *Acta Mech*. 1991;87(3):197-217.

74. Dyskin AV, Muhlhaus H-B, Pasternak E. *Bifurcation and Localisation Theory in Geomechanics*. Leiden, the Netherlands: CRC Press; 2021.

75. Mühlhaus H-B, Vardoulakis I. The thickness of shear bands in granular materials. *Geotechnique*. 1987;37(3):271-283.

76. Muhlhaus H, Moresi L, Gross L, Grotowski J. The influence of non-coaxiality on shear banding in viscous-plastic materials. *Granul Matter*. 2010;12(3):229-238. https://doi.org/10.1007/s10035-010-0176-9.

77. Shi J, Guo P, Stolle D. Micromechanical analysis of non-coaxiality between stress and strain increment in granular materials. *Acta Geotech*. 2020;15:2559. https://doi.org/10.1007/s11440-020-00923-x.

78. Ai J, Langston PA, Yu H-S. Discrete element modelling of material non-coaxiality in simple shear flows. *Int J Numer Anal methods Geomech*. 2014;38(6):615-635.

79. Li X, Yu HS, Li XS. Macro–micro relations in granular mechanics. *Int J Solids Struct*. 2009;46(25-26):4331-4341.

80. Chambon R, Caillerie D, El Hassan N. One-dimensional localisation studied with a second grade model. *Eur J Mech*. 1998;17(4):637-656.

81. Desrues J, Chambon R, Mokni M, Mazerolle F. Void ratio evolution inside shear bands in triaxial sand specimens studied by computed tomography. *Geotechnique*. 1996;46(3):529-546. https://doi.org/10.1680/geot.1996.46.3.529.

82. Mahmood Z, Iwashita K. Influence of inherent anisotropy on mechanical behavior of granular materials based on DEM simulations. *Int J Numer Anal methods Geomech*. 2010;34(8):795-819.

83. Hosseininia ES. Investigating the micromechanical evolutions within inherently anisotropic granular materials using discrete element method. *Granul Matter*. 2012;14(4):483-503.

84. Pardoen B, Bésuelle P, Dal Pont S, Cosenza P, Desrues J. Accounting for small-scale heterogeneity and variability of clay rock in homogenised numerical micromechanical response and microcracking. *Rock Mech Rock Eng*. 2020;53(6):2727-2746. https://doi.org/10.1007/s00603-020-02066-7.

85. Galvanetto U, Aliabadi MH. *Multiscale Modeling in Solid Mechanics: Computational Approaches*. London, UK: Imperial College Press; 2010.

86. Nguyen T-K Failure analysis of pressurized hollow cylinder made of cohesive-frictional granular materials. In Modern Mechanics and Applications. Springer. 2022:707-715. https://doi.org/10.1007/978-981-16-3239-6_54

87. Nguyen GD, Nguyen CT, Nguyen VP, Bui HH, Shen L. A size-dependent constitutive modelling framework for localised failure analysis. *Comput Mech*. 2016;58(2):257-280. https://doi.org/10.1007/s00466-016-1293-z.